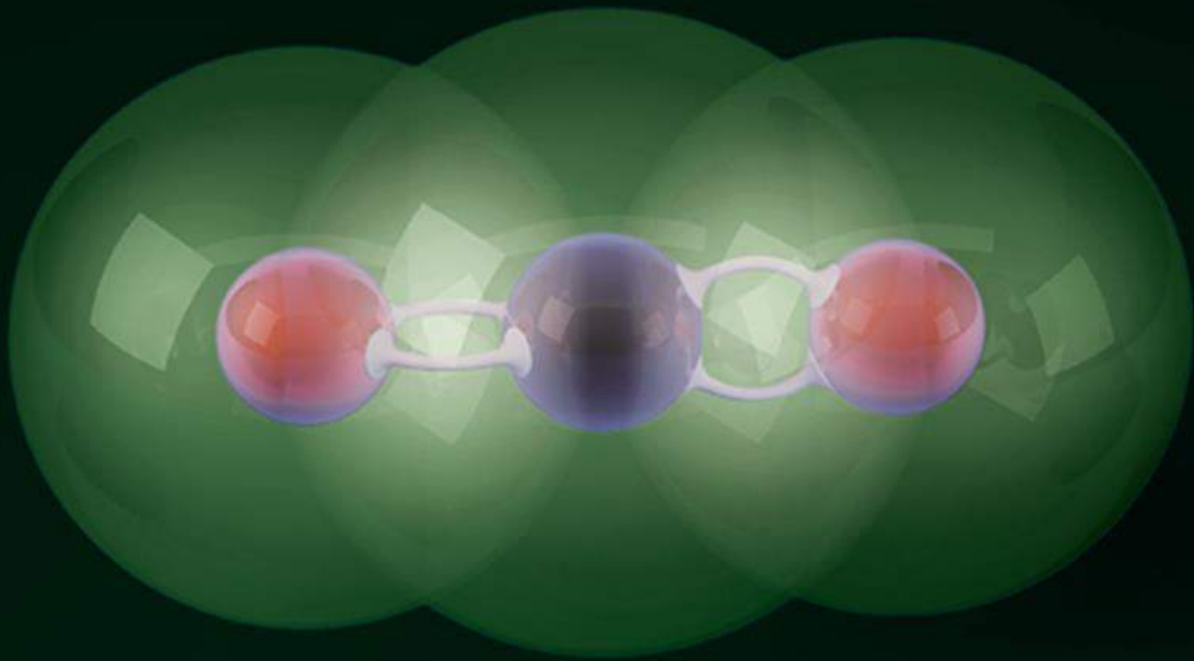


Electrochemical Reduction of CO₂ to CO in Membrane Electrode Assembly (MEA) Setup



Electrochemical Reduction of CO₂ to CO in Membrane Electrode Assembly (MEA) Setup

By

H.S.S. Al-Gariri

in partial fulfilment of the requirements for the degree of

Master of Science
in Sustainable Energy Technology

at the Delft University of Technology
to be defended publicly on Monday July 12, 2021, at 09:00 AM

Supervisors: Prof. dr. J.J.C Geerlings,
S. Chandrashekar

Thesis committee: Dr. T. Burdyny,
Dr.ir. David A. Vermaas

Acknowledgements

My research is incomplete without thanking the people who have been there for me during the entire process. The last year has definitely been an unforgettable period of my life. To have a global pandemic outbreak in the second week of the project is not the best start anyone could wish for. Nevertheless, I am grateful that I had great people who never stopped sharing the positive vibes in those hard times.

First of all, I would like to thank my daily supervisor Sanjana for all the ideas generated, planning advice, and even listening to my frustrations during Skype discussions. Your constant motivation has kept me focused throughout the project.

Also, I would like to thank my thesis supervisor Hans for the valuable insights and solutions to problems met along the way.

Additionally, I would like to recognize the invaluable assistance from the MECS group members who have been involved with my work. Giorgio for helping me with the COMSOL model. Erdem, Hugo, Kailun, Marijn and Sid for all the discussions and assistance during lab experiments. Herman and Joost for helping with the technical issue in the lab.

Last but not least, special thanks my friends and family for their constant love and support.

Abstract

The global concern of the increasing levels of CO₂ is growing quickly in the recent years. Therefore, a lot of research is currently underway with respect to closing the carbon cycle. The electrochemical reduction of CO₂ is a promising technology that could help utilize the CO₂ as a feedstock to produce chemicals and fuels, while storing the excess energy generated from renewable energy sources in chemical bonds. Due to its simplicity and economic feasibility, the conversion of CO₂ to CO has a high potential in the industrial market. Membrane Electrode Assembly (MEA) is an interesting electrochemical reactor configuration to produce CO on industrial scale due to the low ohmic losses and reduced risk of catalyst poisoning. Optimizing the catalyst and operating conditions are key steps towards the commercialization of the process. This research focuses on understanding the influence of different process parameters on the CO selectivity while analyzing the performance challenges. Multiple inlet flow rates of CO₂ were tested at different current densities to evaluate its impact on the faradaic efficiency. The experiments were performed using KOH-exchange MEA cell with gas diffusion electrodes and Sustainion membrane. Since the product of interest is CO, Ag-based catalyst layer was sputtered on the gas diffusion electrode. The cathodic products were identified and quantified using gas chromatograph. The experimental results have shown that increasing current density resulted in lower CO selectivity, while the inlet flow rate did not have a significant effect. It was also shown that the cell could not achieve higher than 200mA/cm² due to the accumulation of salts blocking the gas flow channel.

On top of that, a simple 2D model was developed in COMSOL Multiphysics to understand the mass transport and concentration distribution in the gas flow channel. The model was not able to simulate the complexities of the electrochemical process and represented an ideal plug flow reactor. It is understood that the incorporation of reaction kinetics and current distribution is necessary to replicate the real scenario.

Contents

Contents.....	iv
List of Figures	vi
1. Introduction	1
1.1 Background	1
1.2 Research objectives	2
1.3 Report overview	2
2. Theory	3
2.1 General overview of CO ₂ reduction	3
2.1.1 Electrochemical half-reactions	3
2.1.2 CO ₂ RR products	4
2.1.3 Hydrogen evolution reaction	4
2.1.4 Catalysts	5
2.2 CO ₂ reduction reactor design.....	6
2.2.1 H-cell	6
2.2.2 Membrane electrode assembly	7
3. Experimental Methods	11
3.1 Experiment plan	11
3.2 Preparation of electrode and electrolyte	11
3.3 Electrochemical cell configuration (MEA)	12
3.4 Experimental Setup	15
4. Theoretical Model Description.....	23
4.1 Finite element method	23
4.2 Model parameters	23
4.2.1 Geometry	23
4.2.1 Species diffusivity	25
4.3 Model physics.....	25
4.3.1 Brinkman equation	25
4.3.2 Transport of concentrated species	26
4.3.3 Electrode Surface Coupling.....	27
5. Results and discussions	28
5.1 Experimental results	28
5.1.1 Chronopotentiometry.....	28

5.1.2 Mass flow meter (MFM)	29
5.1.3 Faradaic efficiency (FE).....	34
5.1.4 Performance Challenges.....	37
5.2 Model Results.....	38
5.2.1 Model validation.....	38
5.2.2 Parametric Analysis.....	40
5.2.3 Temperature Influence on Cell Performance.....	42
6. Conclusions and Recommendations.....	45
6.1 Conclusions	45
6.2 Recommendations	45
7. Bibliography.....	47
Appendix	52
A. MFM data.....	52
B. Faradaic efficiencies	54
C. Cell potentials	62

List of Figures

Figure 1: Overview of selected products of CO ₂ electrochemical reduction, in comparison with the current industrial methods. [10].....	2
Figure 2: Volcano plot of current density vs binding strength of CO. Adapted from Zhu et al [29]	6
Figure 3: Schematic of a lab-scale H-cell for CO ₂ electrolysis. Retrieved from [37]	7
Figure 4: Schematic of zero-gap membrane (or membrane electrode assembly) reactor. 3D view of the cell is presented on the left, and a cross-sectional view is shown on the right. Adjusted from [42].....	8
Figure 5: Cross-sectional illustration of various CO ₂ reduction cell designs. Retrieved from Weber et al [44]	8
Figure 6: Cross-sectional schematic of gas diffusion electrode (GDE) used for CO ₂ reduction. Retrieved from [46]	9
Figure 7: Sigracet 39BC carbon paper GDL. Left: Blank GDL. Right: after sputtering 150 nm Ag catalyst layer on the microporous layer of the GDL. The corners of the MPL were taped against the sputtering sample holder and hence the MPL is visible.	12
Figure 8: Schematic view of the MEA configuration used in the experiments.....	13
Figure 9: Picture of the MEA configuration components of CO ₂ electrolyzer used in experiments. A) Cathodic titanium plate and flow field, B) PTFE gasket, C) Gas diffusion electrode (Sigracet 39BC) with 100nm Ag sputtered, D) Sustainaion AEM (dry after being used in experiment), E) Nickel foam used as anode, F) Silicon gasket, G) Anodic stainless-steel plate with 5cm ² flow field.	14
Figure 10: MEA cell after assembly. The blue and red wires are used for electrical connections.....	14
Figure 11 : Flow diagram representing the main components of the experimental setup.....	15
Figure 12: Bronkhorst High-Tech Mass Flow Controller (MFC)	16
Figure 13: PARAFILM Semi-transparent film used to cover anolyte container.....	16
Figure 14: Liquid trap.....	17
Figure 15: Bronkhorst Mass flow meter (MFM) [59]	17
Figure 16: Gas Chromatograph	18
Figure 17: PARSTAT® MC 2000A.....	19
Figure 18: Picture of the leak detector used for small leaks detection	21
Figure 19: Anolyte leakage from the liquid compartment	22
Figure 20 : A schematic representing a top view of 2D straight flow channel of MEA cell with GDL and catalyst layer.....	24
Figure 21: Chronopotentiometry tests at fixed flow rate 30sccm; and variable current densities.....	29
Figure 22: Plots of the outlet mass flow rate over the time of experiments at fixed current density of 100 mA/cm ² and variable inlet flow rate.....	30
Figure 23: Plot of the average outlet mass flow rate after each GC injection; at fixed current density of 200 mA/cm ² and variable inlet flow rates	31
Figure 24: Picture of the cathode-side gas flow channel after conducting CO ₂ RR experiment at 200mA/cm ² and 40 sccm. Large salt crystals are clearly visible.....	32
Figure 25: Pictures of the back side of the GDL after conducting CO ₂ RR experiments at 200mA/cm ² and different inlet flow rates. A) at 20 sccm, B) at 40 sccm.....	32

Figure 26: Flow rate loss over total current densities at different inlet flow rates.	33
Figure 27: Faradaic efficiency of the gas products of CO ₂ RR on Ag at 50 mA/cm ² and 20 sccm	34
Figure 28: FE for CO and H ₂ production over total current density at different inlet flow rates	35
Figure 29: FE of the gas products of CO ₂ RR on Ag sample at 200 mA/cm ² and 40 sccm.	36
Figure 30: FE loss over total current densities at different inlet flow rates.....	37
Figure 31: The mesh independence study for model validation, monitoring the molar concentration of CO ₂ near the outlet of the channel; Current density: 100mA/cm ² , inlet flow rate: 30sccm.....	39
Figure 32: Mole fraction of CO ₂ along the width of cathode at a fixed current density (300 mA/cm ²) and four different inlet flow rates. The x axis starts from the catalyst layer @ x=0, and ends at the backside of the flow channel @ x=1.325	40
Figure 33: Mole fraction of CO along the width of cathode at fixed current density 300mA/cm ² . The x axis starts from the catalyst layer @ x=0, and ends at the backside of the flow channel @x=1.325	41
Figure 34: Mole fraction of CO ₂ along the width of cathode at fixed flow rate 20sccm. The x axis starts from the catalyst layer @ x=0, and ends at the backside of the flow channel @x=1.325	42
Figure 35: Molar concentration of CO ₂ along the width of cathode at different operation temperatures. The x axis starts from the catalyst layer @ x=0, and ends at the backside of the flow channel @x=1.325	43
Figure 36: Molar concentration of CO along the width of cathode at different operation temperatures. The x axis starts from the catalyst layer @ x=0, and ends at the backside of the flow channel @x=1.325	43
Figure 37: Average outlet mass flow rate after each GC injection; at fixed current density of 50 mA/cm ² and variable inlet flow rates	52
Figure 38: Average outlet mass flow rate after each GC injection; at fixed current density of 150 mA/cm ² and variable inlet flow rates.	53
Figure 39 : FE of the gas products of CO ₂ RR on Ag sample at 50 mA/cm ² and 20 sccm.	54
Figure 40: FE of the gas products of CO ₂ RR on Ag sample at 100 mA/cm ² and 20 sccm.	54
Figure 41: FE of the gas products of CO ₂ RR on Ag sample at 150 mA/cm ² and 20 sccm.	55
Figure 42: FE of the gas products of CO ₂ RR on Ag sample at 200 mA/cm ² and 20 sccm.	55
Figure 43: FE of the gas products of CO ₂ RR on Ag sample at 50 mA/cm ² and 30 sccm.	56
Figure 44: FE of the gas products of CO ₂ RR on Ag sample at 100 mA/cm ² and 30 sccm.	56
Figure 45: FE of the gas products of CO ₂ RR on Ag sample at 150 mA/cm ² and 30 sccm.	57
Figure 46: FE of the gas products of CO ₂ RR on Ag sample at 200 mA/cm ² and 30 sccm.	57
Figure 47: FE of the gas products of CO ₂ RR on Ag sample at 50 mA/cm ² and 40 sccm.	58
Figure 48: FE of the gas products of CO ₂ RR on Ag sample at 100 mA/cm ² and 40 sccm.	58
Figure 49: FE of the gas products of CO ₂ RR on Ag sample at 150 mA/cm ² and 40 sccm.	59
Figure 50: FE of the gas products of CO ₂ RR on Ag sample at 200 mA/cm ² and 40 sccm.	59
Figure 51: FE of the gas products of CO ₂ RR on Ag sample at 50 mA/cm ² and 50 sccm.	60
Figure 52: FE of the gas products of CO ₂ RR on Ag sample at 100 mA/cm ² and 50 sccm.	60
Figure 53: FE of the gas products of CO ₂ RR on Ag sample at 150 mA/cm ² and 50 sccm.	61
Figure 54: FE of the gas products of CO ₂ RR on Ag sample at 200 mA/cm ² and 50 sccm.	61
Figure 55: Average cell potentials versus total current densities of all experiments	62

1.Introduction

1.1 Background

Since the industrial revolution in the 18th century, the atmospheric concentration of carbon dioxide (CO₂) and greenhouse gases (GHG) has rapidly increased. This was mainly driven by the high demand for energy which was powered by fossil fuels. The levels of CO₂ in atmosphere have reached alarming levels, currently amounting to around 419 ppm as per April 2021 [1]. The recent excessive CO₂ emissions has a significant contribution towards climate change effects, such as the rising global average temperatures of air and oceans, extensive melting of massive ice fields and glaciers around the world, and the global rising of sea levels [2].

In order to mitigate climate change, several approaches have been considered for a long time, involving the improvement of energy efficiency, large deployment of renewable energy sources, in addition to carbon capture and sequestration (CCS) [3]. Most of these technologies have played a positive role in the process of mitigation although they are followed by their own drawbacks. For instance, it is cited that CCS alone could help reducing average CO₂ emissions by 19%, but such technologies come with large cost [4].

One of the most promising technologies to address global warming in the recent years is the direct conversion of CO₂ into fuels and value-added products, such as carbon monoxide (CO) [5] [6], formic acid [7], methanol [8], and ethylene [9]. The electrochemical conversion of CO₂ offers a solution to tackle the intermittency problem associated with renewable energy sources, mainly wind and solar, by storing the energy in the form of chemical bonds. Figure 1 presents a comparison between the electrochemical and thermochemical routes to produce selected C-products [10]. It is evident that the current industrial production methods are primarily fossil-fuel based and require high pressures and temperatures. The electrochemical CO₂ reduction can provide a sustainable pathway to produce these hydrocarbons at very mild conditions.

Scale is a critical factor for the electrochemical process to replace the current fossil fuel based infrastructure. Therefore, the electrochemical reaction needs to be performed at high production rates in order to be economically feasible. Optimized reactors, catalysts and operating conditions are required to improve the efficiency of the process. According to Kenis et al, the CO₂ reduction reaction needs to reach high current densities (a minimum of 100 mA/cm²) in order to make an attractive business case. [11]

The adoption of membrane electrode assembly (MEA) cells is gaining a lot of research interest recently in the fields of green hydrogen and fuel cells. This is because they are capable of achieving high current densities in comparison to the typical H-cell reactors, due to the significant reduction in ohmic losses. It has been proven that MEA's can improve the current densities by an order of magnitude [12], but further research is needed to optimize the cell configuration, components, and operating conditions specifically for the electrochemical conversion of CO₂.

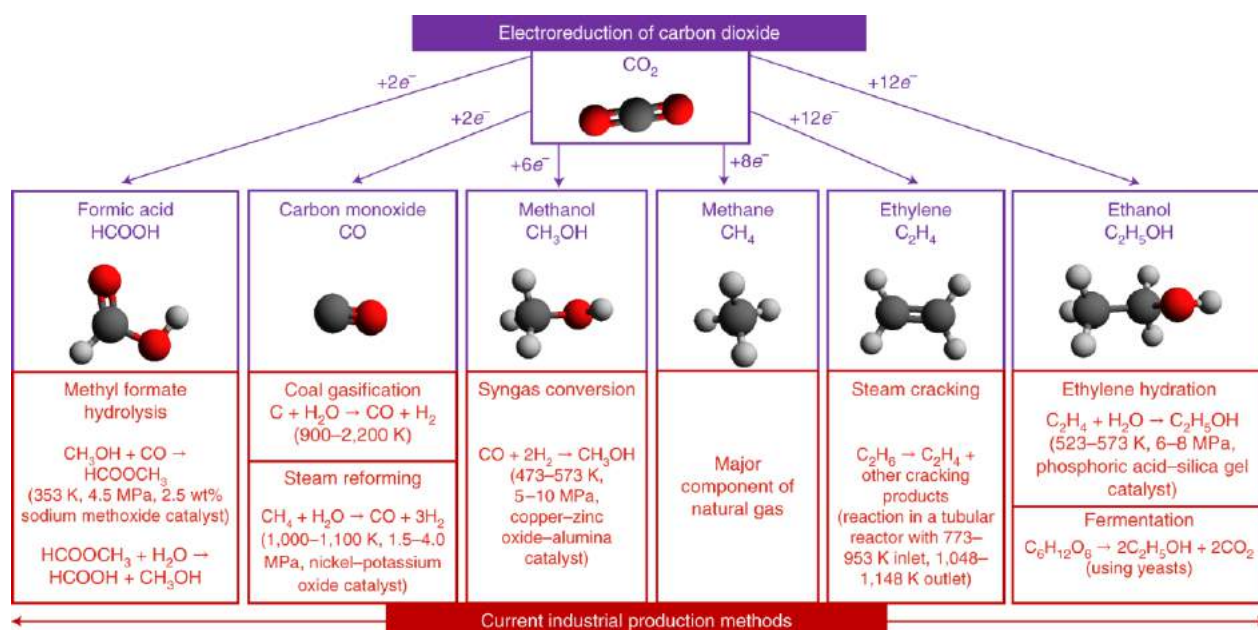


Figure 1: Overview of selected products of CO₂ electrochemical reduction, in comparison with the current industrial methods. [10]

1.2 Research objectives

The main goal of this research is to understand and optimize the operating conditions of the electrochemical reduction of CO₂ to CO on silver-based catalysts using MEA setup. This is done by testing the performance of the cell experimentally under different current densities and inlet flow rates of CO₂. Also, the research is complemented by a theoretical model that aims to analyze the mass transport inside the gas flow channel of MEA. The model should help identify the optimal flow rates needed to overcome any mass transport limitations. The research objectives can be summarized in the following questions:

- What are the ideal operating conditions to obtain high CO selectivity?
- What are the critical factors to improve the reaction rates and overall product selectivity?
- What minimum inlet flow rate of CO₂ is required to make sure the reaction is not limited by mass transport at any point within the gas flow channel?

1.3 Report overview

The report is set up as follows: An overview of the basic principles of CO₂ reduction and the electrochemical reactors will be given in Chapter 2. In chapter 3, the experimental methods conducted in this research will be presented together with a description of the theoretical model developed. Chapter 4 displays the results of both experimental work and theoretical model, while Chapter 5 summarizes the conclusions of the thesis and suggests recommendations for future work.

2. Theory

This study is investigating the electrochemical conversion of CO₂. Therefore, this chapter will start with the basic principles of the electrochemical reactions to produce various products. Next, a general overview of the electrochemical reactors used for CO₂ reduction. Finally, an overview of the membrane electrode assembly (MEA) reactor configuration will be presented, with the function and working principles of each component.

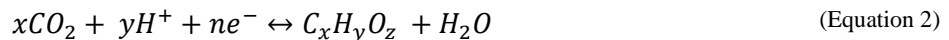
2.1 General overview of CO₂ reduction

The electrochemical reduction of CO₂ has been investigated for more than four decades in different types of reactors and with different catalysts [13]. The electrolytic reaction is performed in an electrolytic reactor which consists of four main components. The first component is the cathode (negative electrode) that reduces the CO₂ into carbon-based products. The second component is the anode (positive electrode) in which a counter reaction occurs to supply electrons and protons to the cathode side. The counter reaction is usually the oxygen evolution reaction (OER), but it may also be a mixture of organic compounds oxidation reactions [14]. Third component is an electrolyte solution that serves as a medium for ion transport. The electrolyte can either be solid or liquid. Fourth component is a voltage source to transport electrons through an external circuit from the positive electrode (anode) to the negative electrode (cathode).

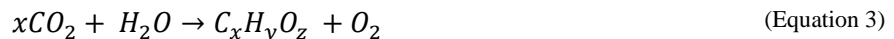
2.1.1 Electrochemical half-reactions

The electrochemical CO₂ reduction reaction (CO₂RR) is a redox reaction, which is defined as the electron transfer reaction between the reductant and the oxidant. In this kind of reactions, the reductant (reducing agent) gives up electrons at the anode and is oxidized, while the oxidant (oxidizing agent) takes up electrons at the cathode and is reduced. These two half-reactions are naturally in thermodynamic equilibrium and maintain electroneutrality.

The overall conversion occurring in the electrochemical CO₂ reduction cell is the sum of two half-reaction. Water oxidation, also known as Oxygen Evolution Reaction (OER), at the anode side of the cell (Equation 1), and the CO₂ reduction reaction (CO₂RR) at the cathode side (Equation 2).



By adding Equation 1 and Equation 2, we get the total transformation equation:



Equation 3 requires a large amount of energy to proceed forward in the form of electricity, which is converted and stored in the chemical bonds of the produced molecules. Catalysts are needed to overcome the significant kinetic barriers in both half-reactions, OER and CO₂RR. Although each reaction has its standard potential, excess voltage (known as overpotential) is needed above the thermodynamic requirement in order for the reaction to proceed forward. The role of catalysts is reducing the overpotential to improve the energy efficiency as well as enhancing the selectivity towards specific products. More details about the catalysts will be discussed in a separate section. In this thesis, the CO₂RR is the main reaction of interest, while OER is considered as a complementary reaction.

2.1.2 CO₂RR products

It is possible to reduce CO₂ to a variety of gaseous and liquid products, depending on the operating conditions (temperature, pressure, applied potential), as well as the reactor design parameters (catalyst, electrode material or electrolyte composition) [15]. These variables dictate the number of electrons transferred at the cathode between the CO₂ molecule and the surface of electrode. The most common products include carbon monoxide (CO), methane (CH₄), ethylene (C₂H₄), formic acid (HCOOH), methanol (CH₃OH), ethanol (C₂H₅OH), and propanol (C₃H₇OH). Table 1 summarizes the half-cell electrochemical reactions to produce the aforementioned products, together with the corresponding thermodynamic electrode potentials versus the standard hydrogen electrode (SHE) under standard operating conditions, including pH 0 [16]. The seven major products are followed by hydrogen evolution reaction (HER), which is the competing undesirable reaction that occurs if CO₂ reduction is performed in an aqueous environment. In addition, there are more than 15 other products reported from CO₂RR, such as acetaldehyde, ethylene glycol, glyoxal, etc. However, it is reported that the amounts produced are insignificant [17] [18].

Table 1: Common CO₂RR products and their half-cell electrochemical reactions. [16]

Cathodic CO ₂ RR half-cell electrochemical reactions	Potential (V vs SHE)
$CO_2 + 2H^+ + 2e^- \leftrightarrow CO(g) + H_2O(l)$	-0.106
$CO_2 + 2H^+ + 2e^- \leftrightarrow HCCOH(l)$	-0.250
$CO_2 + 6H^+ + 6e^- \leftrightarrow CH_3OH(l) + H_2O(l)$	0.016
$CO_2 + 8H^+ + 8e^- \leftrightarrow CH_4(g) + 2H_2O(l)$	0.169
$2CO_2 + 12H^+ + 12e^- \leftrightarrow C_2H_4(g) + 4H_2O(l)$	0.064
$2CO_2 + 12H^+ + 12e^- \leftrightarrow C_2H_5OH(l) + 3H_2O(l)$	0.084
$3CO_2 + 18H^+ + 18e^- \leftrightarrow C_3H_7OH(l) + 5H_2O(l)$	0.095
Water reduction half-reaction	
$2H_2O + 2e^- \leftrightarrow H_2(g) + 2OH^-$	0.000

2.1.3 Hydrogen evolution reaction

As presented in Table 1, there is an alternative reduction reaction that occurs at the cathode of CO₂ electrolyzers, which is the reduction of water or the Hydrogen Evolution Reaction (HER). Equations 4 & 5 describe the HER in acidic and alkaline environments, respectively [19].





The CO₂RR and HER are considered to be in competition for the surface absorbed protons since both reactions utilize protons/water as reactant and occur at comparable potentials. The equilibrium potential for H₂ evolution is 0 V versus SHE, which causes low selectivity towards the desired products.

From the half-cell electrochemical reactions, it could be expected that the CO₂RR would require an acidic media, due to the high proton concentration needed. However, it has been shown that alkaline environment can also favor the CO₂ reduction. The required proton supply is provided by the adjacent H₂O molecules during operation of the electrochemical reactor, and thereby producing hydroxyls (OH⁻). Although operating in a low pH allows for more H⁺ access and easier OH⁻ disposal, it promotes the competing HER over CO₂RR. In general, the local pH near the surface of cathode should increase during the reaction in both media, since more H⁺ gets consumed in acidic environment, and more OH⁻ is produced in alkaline environment.

2.1.4 Catalysts

There has been considerable research focus in literature on methods to enhance different factors in CO₂RR including energy efficiency, product selectivity and conversion rates. In 1985, it was found by Hori et al that CH₄ and C₂H₄ were produced when using Copper (Cu) as a catalyst for CO₂ electrolysis [20]. This breakthrough was followed by several reports evaluating a variety of transition metals and their activity in CO₂ reduction.

There is a large variety of CO₂ reduction catalysts reported in literature, which can be classified in three general groups. The first group include non-metallic catalysts, such as 3-D graphene foam with nitrogen defects [21]. The second include molecular catalysts such as transition-metal-centered molecules [22]. The last and largest group are the metallic catalysts which can be split into three classes: Ion-modified metallic e.g., Ag-O; Bimetallic alloys e.g., AuCu and the monometallic subgroup e.g., Ag, Cu; Nano-structured subgroup e.g., nanoparticles, Nano foam, Nano corals. In this thesis, the main focus is on heterogeneous catalyst since they are more suitable for large-scale application because they are recyclable and cheap.

The product selectivity is mainly dependent on the binding strength of CO intermediate to the transition metal (catalyst) surface [23]. Metals that bind CO intermediate strongly (e.g., Platinum (Pt), Iron (Fe), Nickel (Ni), etc.) produce only hydrogen as the main product [24] [25]. This is because the catalyst surface is poisoned by CO intermediate during the reaction. On the other hand, catalysts that bind CO intermediate weakly, (e.g., Zinc (Zn), Silver (Ag), Gold (Au), etc.) produce carbon monoxide as the main product [25]. The reason for that is the energetically favorable release of CO from the surface of the catalyst. It is important to note that Copper (Cu) has a unique capability to produce higher C products (e.g., methane, alcohols) that need more than 2-electron reduction, due to the fact that it binds CO intermediate at a moderate binding strength [26].

In order to identify the ideal catalyst to selectively produce a certain product, the Sabatier principle makes up an important tool to predict the activity of catalysts [27]. The principle states

that in order to obtain high catalytic activity, the interactions between substrate and catalyst should neither be too strong nor too weak [28]. Figure 2 presents a volcano plot of activity (i.e., electrochemical current density ECR) versus the binding strength of CO, which is a useful visualization of the Sabatier principle. Based on volcano plots, the optimal catalyst is generally on top of the activity volcano. [29]

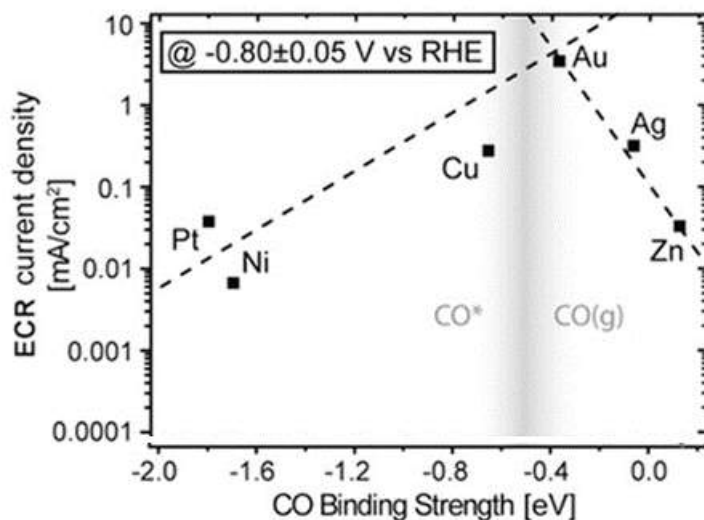


Figure 2: Volcano plot of current density vs binding strength of CO. Adapted from Zhu et al [29]

This study is investigating CO₂RR towards CO production. From the volcano plot in Figure 2, it is understood that Au, Ag and Zn are the most suitable candidates for CO₂ electroreduction to produce CO. It is notable that Ag and Au are comparable in terms of binding energy levels of intermediates, where the latter has the best binding energy for CO production. However, Ag becomes the best option for large scale implementation when considering the trade-off between the activity and material cost [11].

2.2 CO₂ reduction reactor design

The electrochemical research of CO₂ reduction several studied in multiple types of reactors including: H-cell reactors [7], flow cell/microfluidic cell reactors [30], filter press reactors [31], hybrid reactors [32], trickle bed reactors [33], and zero-gap membrane reactors [34] [35] [36].

2.2.1 H-cell

In general, electrochemical reactors can be subdivided into two groups: batch/semi batch cells and continuous flow cell configuration. H-cells (Figure 3) are considered batch reactors, where both planar electrodes cathode and anode are immersed in liquid electrolyte. The feed CO₂ gas is simply bubbled through the cathodic side of electrolyte (catholyte), as illustrated in Figure 3. At the anode side, water gets oxidized to form O₂ through OER, while CO₂ is reduced at the cathode to form C products depending on the catalyst used. The function of membrane is to separate the

anodic and cathodic chambers and preventing the products from crossing to the opposite side of the cell, where they will be reverted back to the initial reactants.

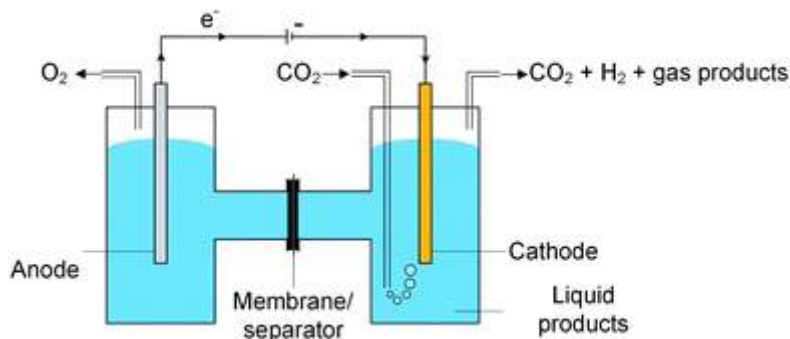


Figure 3: Schematic of a lab-scale H-cell for CO₂ electrolysis. Retrieved from [37]

This type of electrochemical reactor is cheap, simple and allows rapid screening of new catalysts and electrolyte solutions. However, the mass transfer of CO₂ to the surface of cathode is very slow, which keeps the current density limited [38]. Recently, the research focus is directed towards producing elevated current densities (higher than 100 mA/cm²) and operating at system level. Therefore, hybrid reactors and zero-gap membrane reactors are gaining more interest since both configurations are capable of overcoming mass transport limitations of H-cell reactors. This is done by circulating to and away from the electrodes constantly which allows for higher conversion to meet the large scale implementation and commercialization goal [39].

2.2.2 Membrane electrode assembly

This thesis focuses on CO₂ reduction using zero-gap membrane reactor, denoted as membrane electrode assembly (MEA) cell. The configuration has been proven in more mature technologies such as water electrolyzers and hydrogen fuel cells [40]. The main characteristic of MEA configuration is that the cathode and the anode are tightly pressed onto the sides of a membrane. Therefore, the ohmic losses are reduced by the minimization of the gap between electrodes, while keeping both compartments chemically and electrically isolated.

The use of gas diffusion electrodes is favorable over conventional planar electrodes as they allow for higher local concentrations of CO₂ and decrease the mass transport resistances related associated with planar electrodes. This would eventually accelerate the rate of reaction and improve the CO₂ reduction current density [41].

The membrane electrode assembly is typically formed by attaching the membrane in direct contact with both electrodes, as can be seen in the schematic in Figure 4. The figure presents an example of the general setup for MEA cell reactors used for CO₂ reduction to CO, adopted from the work of [42].

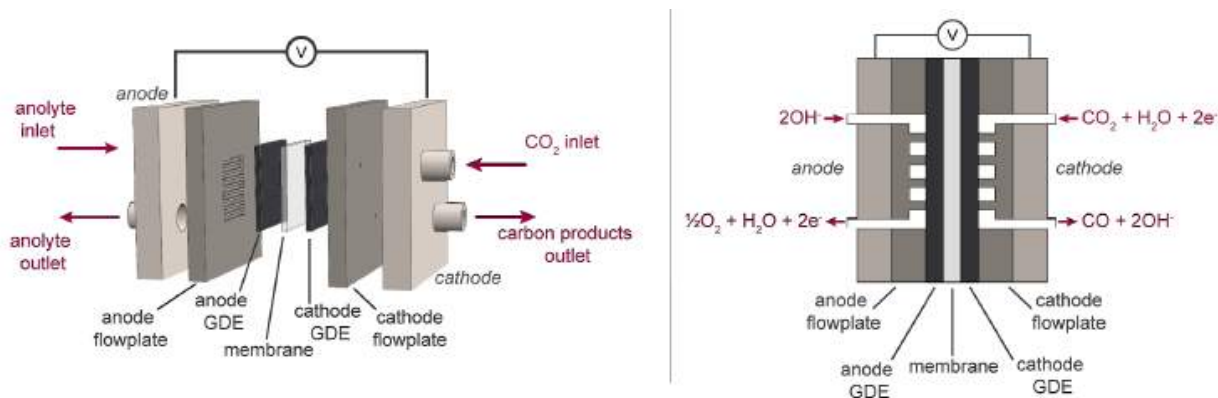


Figure 4: Schematic of zero-gap membrane (or membrane electrode assembly) reactor. 3D view of the cell is presented on the left, and a cross-sectional view is shown on the right. Adjusted from [42].

Multiple configurations and designs have been reported with much debate as to which MEA design is the most efficient for industrial level operation [43] [44]. The graphical illustrations in Figure 5 shows some of the possible variations in the electrochemical cell configuration, as discussed in [44]. Figure 5C and Figure 5D present two promising designs of MEA; “full-MEA” and “exchange-MEA”, respectively as evaluated by Weber et al [44]. The main difference between these configurations is the feed stream of the anode side. Full-MEA is fed by N₂ gas with 100% relative humidity, while liquid exchange solution (anolyte) is fed for the exchange-MEA [44].

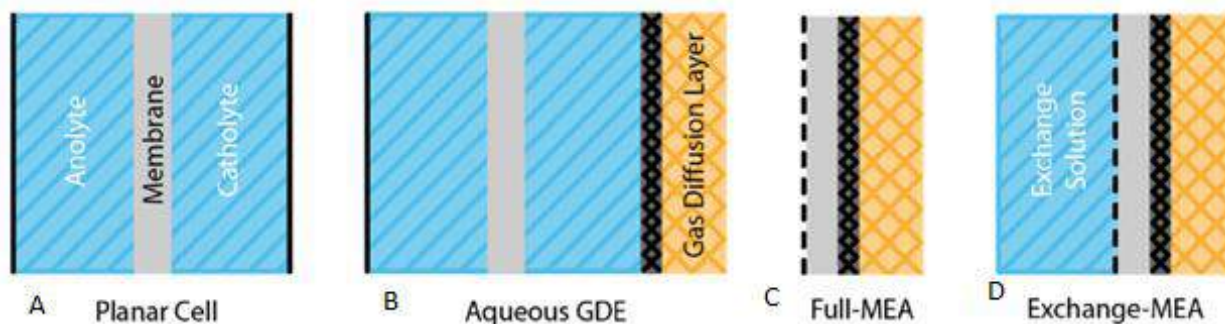


Figure 5: Cross-sectional illustration of various CO₂ reduction cell designs. Retrieved from Weber et al [44]

Although both configurations reduce the ohmic losses significantly across the cell, it was reported that the exchange-MEA outperforms full-MEA in achieving higher total current densities at the same applied cell potential [44]. Also, the availability of liquid anolyte keeps the membrane hydrated which improves the conductivity of ions and reduces the ohmic losses across the cell more in comparison to full-MEA. [37]

This research will be using KOH solution exchange MEA reactor. The detailed setup and components used in this work will be presented in Chapter 3.

Gas diffusion electrode (GDE)

Gas diffusion electrodes (GDE's) are considered a promising approach to enhance the mass transfer of reactants and products while also boosting the reaction rates of CO₂RR [45]. The GDE is typically made up of a gas diffusion layer (GDL), a catalyst layer (CL), and a current collector, as presented in the schematic in Figure 6 [46]. The working mechanism of GDE is that the CO₂ gas diffuses through the GDL to reach the CL at the interface between the electrode and the liquid anolyte solution. It has been found that such GDE electrolysis is capable of improving the rate of reaction by an order of magnitude in comparison to the conventional porous electrode, as it reduces the diffusion length of CO₂. [46] The current collector can either be a separate metal mesh/foam or internally engineered in the structure of the flow channels of electrolyzers [47].

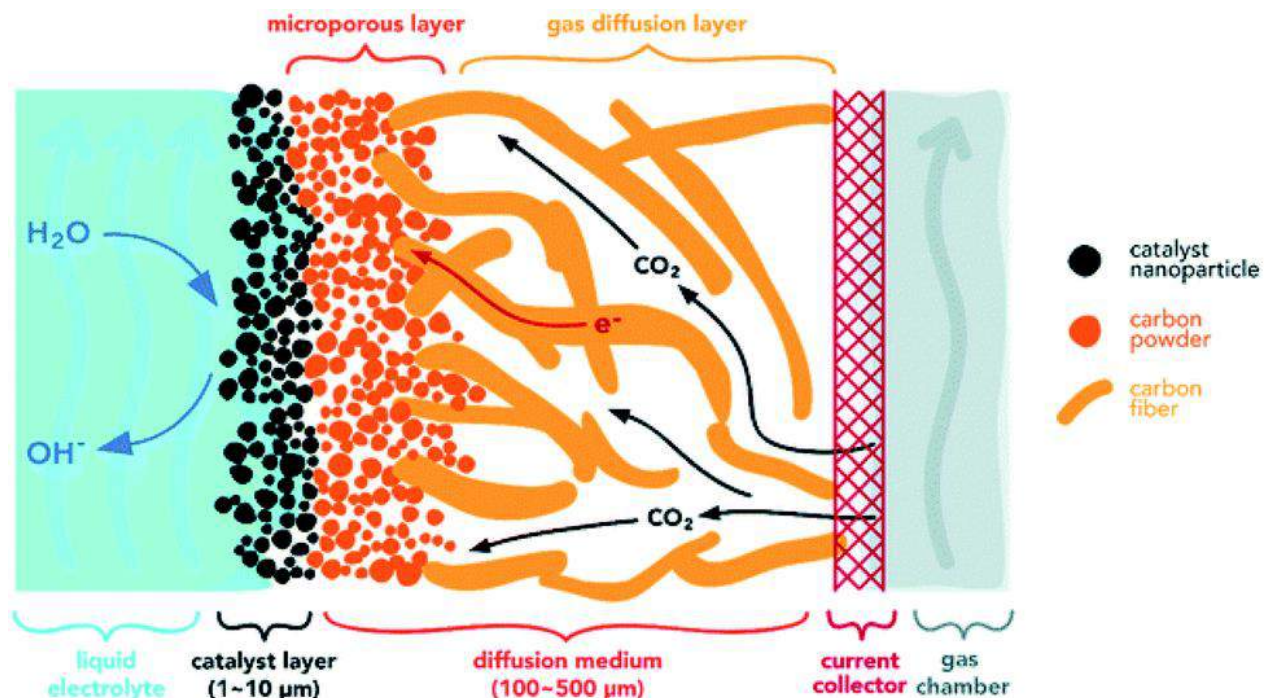


Figure 6: Cross-sectional schematic of gas diffusion electrode (GDE) used for CO₂ reduction. Retrieved from [46]

The GDL consists of a macroporous layer and a microporous layer (MPL). It is important that the GDL needs to be hydrophobic in order to prevent leakage of anolyte to the cathodic (gas) flow channel. The MPL is typically made of a hydrophobic material, such as carbon powder with polytetrafluorethylene (PTFE) treatment. The preparation of catalyst layer is done by depositing the catalytic active phase on the MPL. [48]

Ion exchange membranes

As mentioned previously, semi permeable polymeric membranes are used between the anode and cathode chambers to separate both sides as they are permeable to specific charged ions while being impermeable to ions with different charge or non-charged species. It is common to use monopolar ion exchange membranes in CO₂ electrolyzers. There are two types of monopolar

membranes: cation exchange membranes (CEM) and anion exchange membrane (AEM). There is also a third type of membranes called bipolar membranes (BPM).

As the name suggests, CEM is a membrane that only permeates positively charged ions (cations), such as (H^+ , K^+ , Na^+). On the other hand, the AEM only allows negatively charged ions (anions), such as (OH^- , $HCOO^-$, CO_3^{2-}) to transport across the membrane while blocking other species. The AEM and CEM operate in a similar mechanism but with differently charged species. BPM has a unique structure as it consists of two layers. A cation exchange layer (CEL), and an anion exchange layer (AEL). Between these two layers, there is an intermediate junction layer called “bipolar junction”. While CEM and AEM are meant for the separation of chambers, the BPM has a different mechanism. At the bipolar junction, water dissociation reaction occurs into H^+ and OH^- . The negative CEL is placed facing the cathode side, while the positive AEL should face the anode side. This structure allows for consistent flux of protons and hydroxyl ions along the electric field, while ensuring that the formed ions transport across the respective layer (protons through CEL and hydroxyl through AEL). Therefore, an acid and a base are formed on each side of the membrane and a pH gradient is generated over the BPM. [49]

The selection of membrane is typically based on the combination of choice of catalyst, electrolyte, reaction conditions and the desired products. For instance, in order to produce formate, CEM is ideally selected for its ability to prevent formate anions from penetrating to the anolyte where they will be oxidized back to CO_2 . Also, if the CEM was a proton exchange membrane, the anolyte solution needs to be able to manage high proton concentrations. And these decisions essentially limit the options of anode catalysts to precious noble metals which are very costly, such as Ru and Ir. [50]

System drawbacks

Although it has been proven that such flow cell systems have significant advantages in terms of reaction rates and product yield, this technique has its own problems and challenges which need to be tackled for the process to be intensified in the future. Many sources have reported system issues, such as the crossover of liquid products [51], salt precipitation on the gas flow channel [52], CO_2 cross over to the anode [41] [53], and flooding of the gas diffusion electrode [54]. More details and further analysis for these issues will be given in the coming chapters of this thesis.

3. Experimental Methods

This chapter describes the experimental work of the research. A brief description of the preparation procedures of working electrode (gas diffusion electrode), and electrolyte will be included. Also, the chapter presents the specifications of the MEA cell, the equipment and materials used, together with the complete setup of experiment.

3.1 Experiment plan

The main objective of the experimental study is to understand and optimize the operating conditions of the electrochemical reduction of CO₂ to CO on silver-based catalysts using MEA setup. The flow rate of the CO₂ inlet and the current density applied, have an effect on the selectivity of the products we attain and the amount of CO₂ that is converted to CO. Using chronopotentiometry experiments, it is possible to evaluate the performance of the MEA cell at different CO₂ inlet flow rates and different current densities. The primary plan was to perform 25 experiments where the cell is tested at five different current densities (50,100,150,200,300) mA/cm², and five different CO₂ flow rates (10,15,20,30,40) ml/min. However, only four flow rates were performed due to time constraints and limited lab access. Also, we chose to cancel the 300mA/cm² experiments because of the unexpected high level of salt precipitation. More details on this problem and proposed solutions will be discussed in the Chapter 4.

3.2 Preparation of electrode and electrolyte

Working electrodes are prepared by sputtering a 150nm layer of Ag on top of a (2.5x2.5cm) Sigracet 39BC carbon paper, as presented in Figure 7 . Sigracet 39BC is a non-woven carbon paper gas diffusion media with a Microporous Layer (MPL) that has been PTFE treated to 5% [55]. It is worth noting that the geometric surface area of the gas diffusion electrode is larger than the geometric surface area of cathode flow field to account for CO₂ lateral diffusion. For the counter electrode, a (3x3cm) piece of nickel foam (Ni-4753.005) is used to optimize O₂ evolution at the anode side.

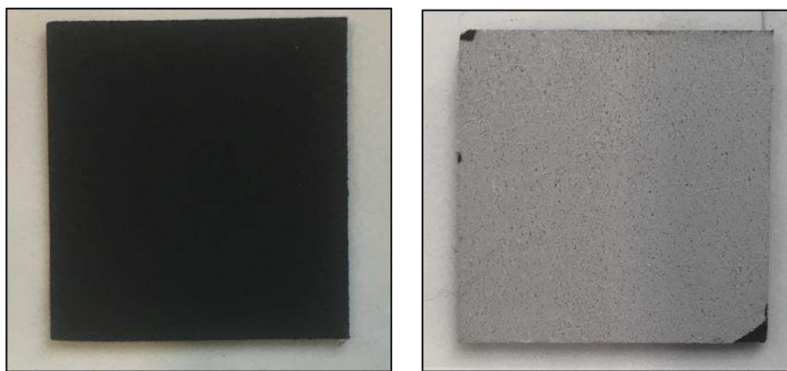


Figure 7: Sigracet 39BC carbon paper GDL. Left: Blank GDL. Right: after sputtering 150 nm Ag catalyst layer on the microporous layer of the GDL. The corners of the MPL were taped against the sputtering sample holder and hence the MPL is visible.

The electrolyte is mainly present as anolyte (electrolyte in the anode compartment) and is typically chosen to be highly alkaline in order to reduce the cell overpotential and promote CO₂RR [56]. The selected electrolyte is 1 molar potassium hydroxide (1M KOH) solution as the anolyte for each experiment. KOH is an alkaline medium which consists of 1M OH⁻ anions and 1M K⁺ cations. The KOH solution is prepared by dissolving 99.99 wt.% KOH pellets (Sigma-Aldrich) in distilled water. For each experiment, 80mL solution is used in the anolyte compartment and is circulated throughout the cell. Theoretically, the pH of the solution is equal to 14, but it might decrease over time due to dissolution of atmospheric and crossed over CO₂. Thus, it is important to check the pH of the solution before a new day of experiments or prepare a fresh solution to ensure near 14-pH mixture is achieved.

Table 2: Preparation of 80mL 1M KOH solution

Target solution	1 M KOH = 1 mol KOH/ L solution
M.W KOH	56.11 g KOH/mol
99.99 wt% KOH	$56.11/0.9999 = 56.12$ g KOH/ mol
Concentration (1M)	56.12 g KOH/L
80 mL solution	$56.12*0.08 = 4.49$ g KOH (99.99) / 80mL H ₂ O

3.3 Electrochemical cell configuration (MEA)

The experimental work of this research was performed using commercially available Dioxide Material 5 cm² CO₂ Electrolyzer Hardware with MEA [57]. The system consists of Titanium anode flow field, 904 L Stainless Steel cathode flow field, nuts, bolts, O-rings, and insulating kit. The MEA configuration is assembled based on the structure shown in the schematic in Figure 8.

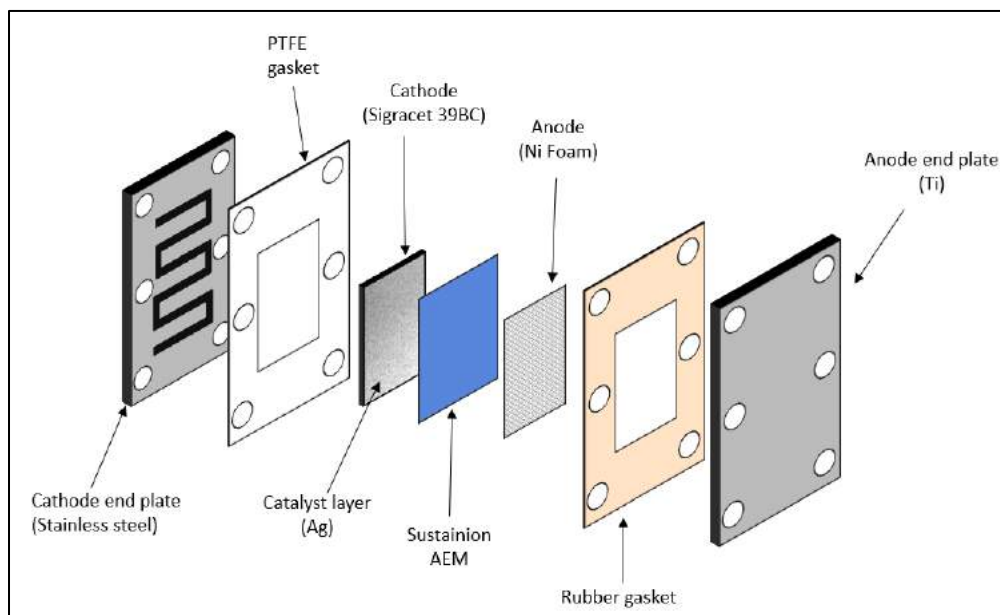


Figure 8: Schematic view of the MEA configuration used in the experiments.

Starting by the titanium anode end plate (Figure 9A), followed by the rubber gasket (Figure 9B) which has a thickness of 500 microns and helps to keep the anode properly placed on the titanium flow field. The anode is a (3x3) cm nickel foam that is placed at the middle of the rubber gasket. The thickness of the anode has to be equal or lower than the gasket to avoid short-circuiting the cell. The used nickel foam (Figure 9C) has a thickness of 300 microns.

After setting the anode, a Sustainion X37-50 anion exchange membrane AEM (Figure 9D) is placed on top of the nickel foam. The AEM has a dry thickness of around 50 microns. The cathode (gas diffusion electrode) is placed on top of the membrane. The cathode used in this work is a carbon GDL paper Sigracet 39BC with 150nm Ag layer sputtered on top of it. This GDL has a thickness of 325 microns. In general, the GDL allows CO₂ to transport freely via the large pores of the carbon paper backing on the gas side. To prevent liquid crossover, the liquid side of the GDL consists of a so-called microporous layer (MPL), which has a much denser structure and higher hydrophobicity. Although the MPL prevents liquid crossover, it is mentioned that this layer can be limiting CO₂ mass transport at high current densities. After traveling past the GDL it is not sure whether CO₂ stays in a gaseous phase or undergoes short distance dissolution before it reaches the Ag catalyst. According to Smith et al, the CO₂ diffuses through the liquid electrolyte, and the reaction occurs explicitly in the liquid phase. [58]

Finally, PTFE gasket with a thickness of 500 microns is placed before the final cathode plate closes the cell. Both of the gaskets are used for protection and electrical insulation.

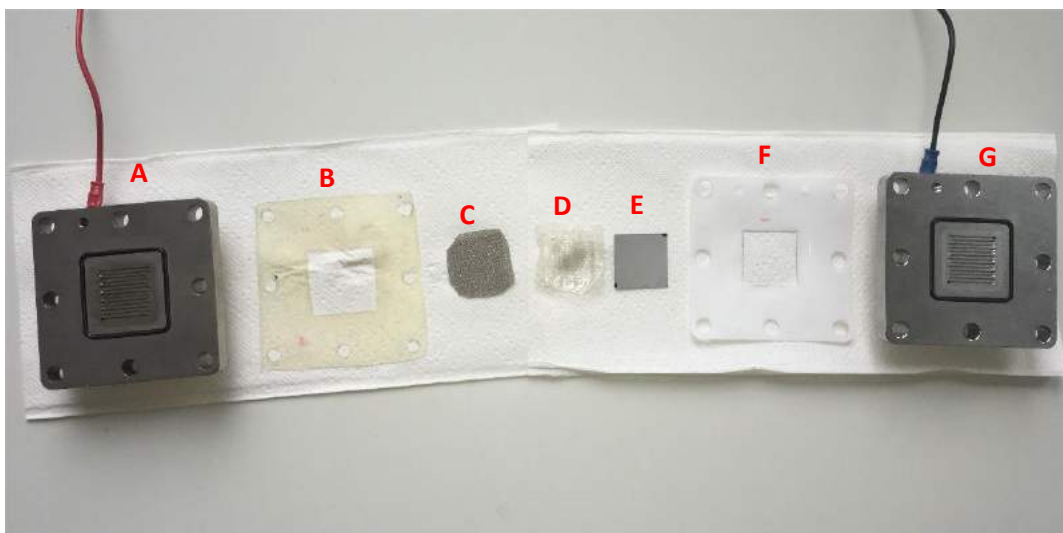


Figure 9: Picture of the MEA configuration components of CO₂ electrolyzer used in experiments. A) Cathodic titanium plate and flow field, B) PTFE gasket, C) Gas diffusion electrode (Sigracet 39BC) with 100nm Ag sputtered, D) Sustinaion AEM (dry after being used in experiment), E) Nickel foam used as anode, F) Silicon gasket, G) Anodic stainless-steel plate with 5cm² flow field.

The entire assembly is sandwiched between the anodic and cathodic plates and fastened with 8 bolts. A dynamic wrench is used to fasten the bolts and compress the components with a torque of 4 Nm. It is important to note that the process of cell assembly should not take more than few minutes to avoid drying of the Sustinaion membrane. Also, a fresh membrane and a new piece of Ag sputtered GDE are used for each experiment to enhance the accuracy of the results.



Figure 10: MEA cell after assembly. The blue and red wires are used for electrical connections

3.4 Experimental Setup

The basic design of the experimental system is depicted in Figure 11. The main components are the CO₂ source, mass flow controller (MFC), gas humidifier, MEA electrolyzer, anolyte solution, peristaltic pump, liquid trap, mass flowmeter (MFM), potentiostat, and the gas chromatograph (GC).

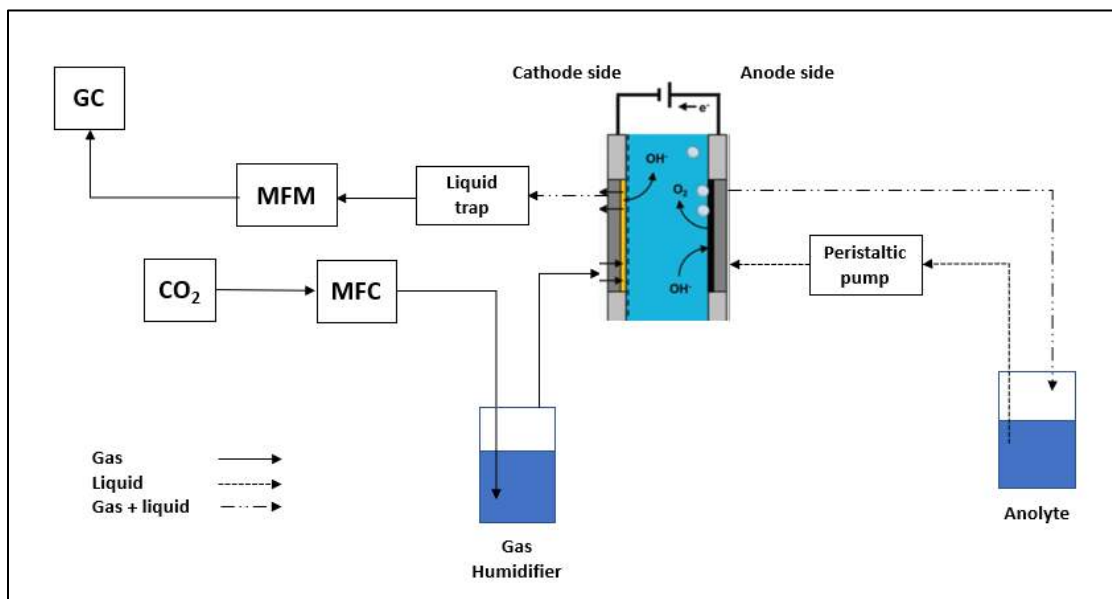


Figure 11 : Flow diagram representing the main components of the experimental setup

The CO₂ flow is supplied from a CO₂ cylinder that contains pure CO₂. The gas inflow of CO₂ is regulated by a mass flow controller (MFC), shown in Figure 12. The function of the MFC is providing accurate tuning of inlet gas flow rate. The flow rate of gas stream is an essential parameter in the calculation of product selectivity, due to the fact that the flowrate dictates the concentration of the formed products in gas phase. Since the cathode chamber is fed by gaseous stream in such an exchange-MEA configuration, the CO₂ needs to be humidified to supply the protons needed for CO₂RR. The feed gas is humidified before entering the cell, by sparging it into a container filled with deionized water (depicted in Figure 11 as Gas Humidifier). The CO₂ flow rates, and the level of humidity are believed to be controlling the concentration of CO₂ and water along the channel, which should have an effect on the rate of reaction [42].



Figure 12: Bronkhorst High-Tech Mass Flow Controller (MFC)

The cathodic flow field of MEA cell is fed with the humidified gas stream, while the anodic flow field is fed with liquid anolyte solution. The anolyte solution is supplied from a 100 mL glass bottle which contains the previously mentioned 1M KOH solution. The peristaltic pump, (Masterflex L/S® Digital Miniflex® Pump, Dual-Channel) is used to circulate the anolyte continuously through the cell at a fixed flow rate of 20 mL/min. This pump utilizes a peristaltic motion to partially compress the pipes and consequently push the anolyte towards the cell at the desired flow rate.

The anolyte solution has to enter the cell from the bottom of the flow channel to top, in order to physically push the gas bubbles formed, mainly through OER, out of the cell. The anodic inlet of the cell is fed from the bottom of anolyte container, while the anodic outlet drips back into the bottle from above the liquid level, as depicted in Figure 11, to allow formed gas products to escape. The anolyte container is sealed using Laboratory Film (Parafilm), shown in Figure 13 in order to avoid acidification of the anolyte solution by atmospheric CO₂.



Figure 13: PARAFILM Semi-transparent film used to cover anolyte container

In order to prevent liquids from entering the MFM and GC, the humidified product stream from the cathodic outlet is passed through an empty vial (shown in Figure 14) in which the liquid is

trapped. It can be seen in Figure 14 that almost half of the vile is filled with small beads to reduce the dead volume which should help to obtain satisfactory GC peak resolution. It is important to make sure that the beads do not reach the outlet tubing, as they may contain trapped liquid droplets. Therefore, the liquid trap is glued to a petri dish, using resin glue, to keep the vile in its upright position. Also, the resin glue is used to seal the cover of the vile and the connected tubes for inlet and outlet.

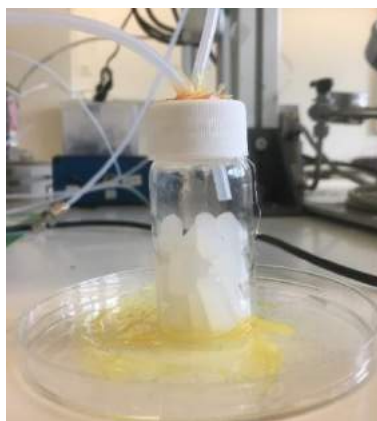


Figure 14: Liquid trap

After trapping the liquids from the product stream, the flow rate of the gaseous products is measured using the MFM. The used device was Bronkhorst® Low- Δp -Flow Mass Flow Meter, which gives precise measurements for applications with low differential pressures. This MFM also has large flow channels to minimize the risk of clogging, facilitate cleaning and purging, and allow for lower pressure drop across the MFM [59]. Prior to connecting the complete setup, the gas flow rate given by MFM is checked by connecting the MFC directly to the MFM. This is done to test the reliability of the MFM reading with respect to the fixed inlet flow rate. In some of the experiments, the MFM reading did not match the MFC reading with direct connection. Therefore, a correction factor was used for the flow rate values to fix the error of MFM readings. Additionally, it is important to check the MFM reading with the complete setup before running the potentiostat to make sure that the system is airtight, and that the inlet flow rate matches the outlet flow rate.



Figure 15: Bronkhorst Mass flow meter (MFM) [59]

Gas chromatography

Gas chromatography is an analytical technique that can separate and detect small molecular weight components in gas phase and classify them quantitatively. The gas chromatograph used in this study is CompactGC4.0 (GAS-Global Analyser Solutions), shown in Figure 16 .

This device operates using three separate columns simultaneously, enabling the system to detect most of the gaseous products injected. The first channel uses flame ionization detection (FID), which is dependent on the variations in boiling point and vapor pressure for products detection. This column (channel) is used for the detection of hydrocarbons in the product stream. Since the expected products in this research are only CO and H₂, the reading of channel 1 is only checked to confirm the unavailability of hydrocarbons, and it is not used for further analysis. The second and third channels operate using thermal conductivity detectors (TCD). These detectors work based on the response of thermal conductivity of the sampled (injected) product gas compared to the carrier gas, which is used as a reference gas. This technique is capable of the detection of wide range of gaseous product due to the fact that each compound has a distinctive thermal conductivity. The two TCD columns in GC work on the same principle but differ in the reference gasses used. The first detector TCD-1, which is connected to channel 2, uses Helium (He) as the reference gas. This makes it suitable for the detection of Oxygen (O₂) and Carbon Monoxide (CO), while being insensitive for Hydrogen (H₂) detection in the product stream. This is because He and H₂ have almost similar thermal conductivities, which minimizes the temperature difference between the sample gas and reference gas. Similarly, the second detector TCD-2 is connected to channel 3 and uses Argon (Ar) as a reference carrier gas. Ar is suitable for detecting H₂ content in the stream, but it has inconsistencies in O₂ detection since Ar and O₂ are comparable in terms of thermal conductivity. Therefore, the selection of appropriate detectors and reference gases in GC is essential in order to determine the concentrations and selectivity of the products.



Figure 16: Gas Chromatograph

Potentiostat

The potentiostat used in this study is PARSTAT® MC 2000A Multichannel potentiostat (Princeton Applied Research) [60]. This potentiostat (Figure 17) is used to perform chronopotentiometry analyses by supplying the working electrode with a fixed current and monitoring the cell potential changes with time. In these studies, the current density is the most common parameter to test the cell performance. Therefore, the applied current to the cell is calculated using the desired current density and the geometric area of catalyst. Equation 6 is used to determine the current needed to reach the required current density, where I is the applied current, j is the current density and A is the geometric surface area of the sample (6.25 cm²).

$$I = j \times A \quad \text{(Equation 6)}$$



Figure 17: PARSTAT® MC 2000A

Gas chromatography is performed simultaneously with the measurements of the potentiostat. The aforementioned detectors (FID, TCD-1 & TCD-2) identify the compounds available in the product stream and determine their concentrations. The concentrations are used to calculate the faradaic efficiency (FE) of each product.

Faradaic efficiency

Faradaic efficiency describes the selectivity of the electrochemical reaction towards producing a specific product. This is done by comparing the number of electrons that are contributing into producing that one product versus the total number of electrons, or total charge, consumed at the working electrode. The GC is injected with a sample from the cathodic outlet of the cell every 5 minutes for a total operation time of 1 hour. The samples pass through each channel and the electrical response from the detectors is examined. The quantity of each product is given as a peak area in the chromatography data system Chromeleon™ software. The peak area is converted into

a concentration in ppm using a calibration file. The following equations describe the method used for FE calculation in this research.

$$FE = \frac{Q_{product}}{Q_{total}} = \frac{Q_{product}}{I \times t} \quad (\text{Equation 7})$$

$$Q_{product} = z \times N_{product} \times F = z \times \frac{P V}{R T} \times F \quad (\text{Equation 8})$$

$$V = \frac{A_{peak}}{\alpha_{product}} \times \varphi \quad (\text{Equation 9})$$

$$FE = \frac{z \times \frac{P}{R T} \times \left(\frac{A_{peak}}{\alpha_{product}} \times \varphi \right) \times F}{I \times t} \quad (\text{Equation 10})$$

In (equation 7), $Q_{product}$ and Q_{total} represent the charge (or number of electrons) used to form a particular product and the total charge used in the experiment, respectively. I is the applied current given from equation 1 in [Ampere], and t is the duration of the experiment in [s]. Equation 8 is used to calculate the number of electrons attributed to the certain product, where z is the stoichiometric number of electrons transferred per mole of the product, $N_{product}$ is the total quantity of product, and F is Faraday's constant (96485 C/mol). In this case, ideal gas law ($N=PV/RT$) is used to determine the term $N_{product}$, in which ($T=298K$, $P=1$ atm and $R=0.082$ L·atm·K⁻¹·mol⁻¹). The volume term in ideal gas equation can be calculated using equation 9, which uses data from GC and MFM. The concentration of desired product is given by dividing the peak area A_{peak} from GC by the calibration curve constant $\alpha_{product}$. This concentration percentage is then multiplied by the outlet flowrate reading given by MFM. The equations can be combined in equation 10 to calculate the faradaic efficiency of the product of interest.

It is important to note that these calculations are done for each injection sample separately. Subsequently, an average value of FE is taken for the samples injected at stable cell potential.

Regular check-up

Before conducting any measurements of potentiostat or GC, the system is tested to address any leakage of liquid or gas. The gas leakage is checked by comparing the fixed inlet flow rate given by the MFC with the outlet flow rate given by the MFM reading. When lower MFM reading is observed, the connections to all components of the system (discussed in chapter 3) are checked to ensure they are properly sealed. Snoop® gas leak detector Figure 18 is used to detect gas leakage in hard-to-reach areas, such as the tubes entering and exiting the gas humidifier. The Snoop leak detector helps creating sustained bubbles even on very small leaks and vertical surfaces. At an early stage, this detector helped identifying the source of gas humidifier leakage. The problem was fixed by using PTFE tape on the tubing transitions of the gas humidifier.



Figure 18: Picture of the leak detector used for small leaks detection

Also, the outlet gas flow rate might be lower than the inlet flow rate due to CO₂ cross over to the anodic side of the cell. This can be observed as gas bubbles in the liquid anolyte stream prior to applying current to the cell. The gas crosses over because of a defect in the Sustainion membrane used in most of the cases, and the cell would need to be disassembled and a new piece of membrane would be used. Hence, it is important to examine the piece of membrane before using, to check if there is any crack on it. Rinsing the membrane with distilled water is a good technique to make sure it is clean and does not have defects. Moreover, the membrane needs to be always wet, as it gets dry very fast (few minutes). Therefore, the membranes should always be stored in a liquid solution, and the process of assembling the cell should be done quickly to prevent dryness of membrane. Once the cell is assembled, it is advised to flow the electrolyte solution immediately to keep the membrane wet.

Another setup-related issue encountered during this work was the leakage of liquid electrolyte at one of the cell connections at the anodic flow field side (see Figure 19). This problem occurred when the white fitting connecting the tubing to the cell is not tight enough, improperly placed or worn out. The latter was the cause of the problem associated with this case depicted in Figure 19. The fitting shown was replaced by a new one that provided a good seal, and the issue was resolved.

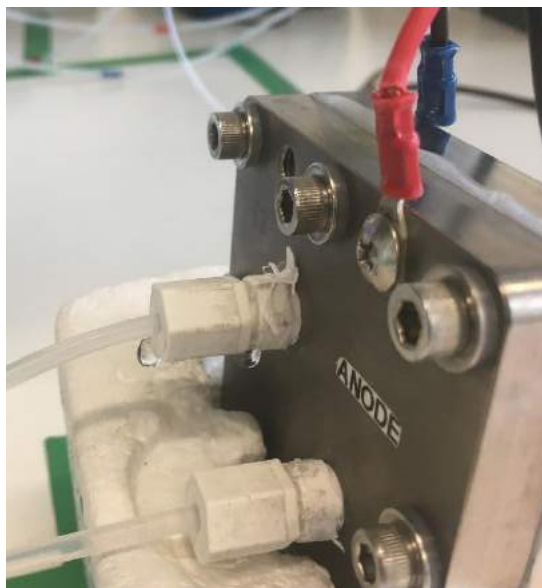


Figure 19: Anolyte leakage from the liquid compartment

4. Theoretical Model Description

This chapter describes a simplified 2D model of the gas input channel at the cathode side of Membrane Electrode Assembly (MEA) cell. Electrochemical CO₂ reduction is a complex process that involves mass transfer, electron transfer, chemical reaction, and adsorption/desorption of reaction intermediates. Understanding mass transport of reactants and products is a critical factor that could help optimizing the CO₂ concentration in the flow channel, which could consequently improve the reaction rates. In order to understand mass transport in the system, it is practical to develop a simplified model that is capable of obtaining quick estimates of species distributions along the gas flow channel.

4.1 Finite element method

In this research, COMSOL Multiphysics 5.5 is used to develop a 2D model of the cathodic flow channel in MEA cell. Most physics interfaces within COMSOL Multiphysics use the finite element method (FEM) to solve the underlying partial differential equations. From a mathematical perspective, the finite element method is based on the principle of minimization, as in minimizing the total energy of the system. The FEM approach works by discretizing the domains of the model into simple and small domains which are usually known as elements. The domain is defined as any connected open subset of a finite-dimensional vector space. The solution is computed by assembling and solving a set of equations over all of the elements of the model. The solution to these equations approximates the true solution to the partial differential equation.

4.2 Model parameters

4.2.1 Geometry

The 2D model is built to represent the gas flow channel of Membrane Electrode Assembly cell used for CO₂ electroreduction to CO using carbon gas diffusion electrode (GDE) and silver catalyst layer. In the real scenario, which is used in the experimental work of this study, a serpentine flow channel is used. However, for the sake of simplicity and the limited scope of the research, a straight flow channel is used to simulate the same process. Figure 20 schematically represents the flow channel of the cell and the Gas Diffusion Layer with the silver Catalyst deposited on it. It is assumed that the reactor is behaving in a steady-state plug-flow regime, and the electrochemical reaction should take place at the catalyst layer. It is also important to note that current distribution is assumed to be uniform, and it is not modelled in this simulation, as it is merely interested in the species transport in the channel.

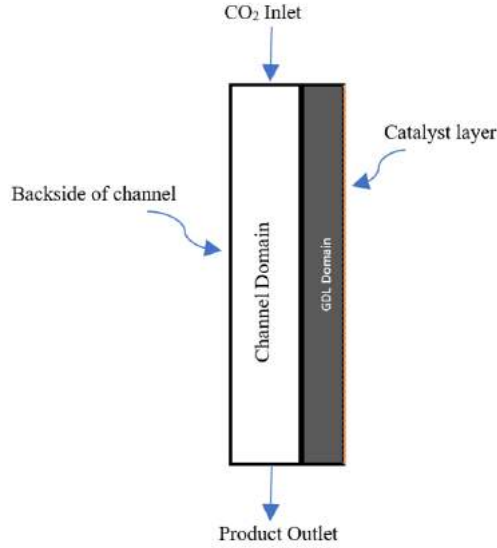


Figure 20 : A schematic representing a top view of 2D straight flow channel of MEA cell with GDL and catalyst layer

The 2D model is developed based on the main geometric details listed in Table 3. The dimensions of the channel and GDL are selected based on the dimensions of the actual components used in the lab. The process conditions listed in Table 3 are similar to the parameters tested in experiments (current densities and flow rates), with the addition of an extra variable parameter which is the cell temperature. The GDL porosity is chosen based on the actual Sigracet39BC GDL specifications [55]. Parametric sweep analysis was performed to simulate all the possible combinations of the parameters. Details of the parametric sweep are discussed in the results chapter.

Table 3: Model input parameters

	Parameter	Value	Unit
Geometry Details	Channel Length	0.02	m
	Channel Width	0.001	m
	Length of GDL	0.02	m
	Thickness of GDL	0.325	mm
Process Conditions	Temperature	(298,323,348)	K
	Current Densities	(50,100,150,200,300)	mA/cm ²
	Inlet Flow Rate	(10,20,30,40)	ml/min
	GDL porosity	80	%

4.2.1 Species diffusivity

Mass diffusivity is a proportionality constant between the molar flux due to molecular diffusion and the concentration gradient of chemical species. It is also known as the driving force for diffusion [61]. The diffusivity of species involved in the model is an important parameter when studying the effect of temperature on the performance of the cell. Based on Nernst-Einstein equation the diffusivity is directly proportional to the diffusive flux, and indirectly proportional to the migration flux. Binary gas phase diffusivities of the model species are estimated using Fuller correlation, given in Equation 11. [61]

$$D_{AB} = \frac{10^{-3} T^{1.75} \left[\frac{1}{M_A} + \frac{1}{M_B} \right]^{0.5}}{P [(\sum \nu)_A^{0.33} + (\sum \nu)_B^{0.33}]^2} \quad (\text{Equation 11})$$

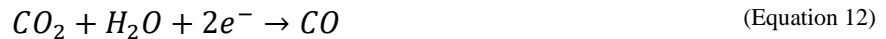
Where D_{AB} is the binary gas phase diffusivity of species A in species B in [cm²/s], T is absolute temperature in Kelvin, P is absolute pressure in atmospheres, M_A, M_B represent the molecular weights of A and B respectively, and $(\sum \nu)_A$ and $(\sum \nu)_B$ are the molecular diffusion volumes in [cm³/g.mol]. The diffusion volumes are obtained from tabulated data in literature [61].

4.3 Model physics

The main processes associated with the functionality of this model can be summarized in the following physics nodes in COMSOL Multiphysics:

1. Fluid flow in porous media (Brinkman equation)
2. Transport of concentrated species.
3. Electrode surface coupling.

The latter physics is applied only on the reaction domain (catalyst layer), while the first two present the interactions and species diffusion between the domains of channel and porous gas diffusion electrode. The modelled reaction is the electrochemical CO₂ reduction to CO:



Thus, the model assumes that all the consumed CO₂ is converted to only CO, which is a simplification made to incorporate the electrical current density in the Electrode Surface Coupling node of COMSOL without simulating the current distribution regime.

4.3.1 Brinkman equation

The fluid flow in porous media is governed by Brinkman equations which are derived from combination of the continuity equation, which deals with conservation of mass, and the equation of motion in for fluid velocity, which concerns the conservation of momentum [62]. This type of

physics is typically used to compute fluid velocity and pressure fields of single-phase laminar flow regime in porous media. Brinkman equation is presented below in Equation 13:

$$\frac{1}{\epsilon_p} \rho (\mathbf{u} \cdot \nabla) \mathbf{u} \frac{1}{\epsilon_p} = \nabla \cdot [-p\mathbf{I} + \mathbf{K}] - \left((\mu\kappa^{-1} + \beta\epsilon_p\rho|\mathbf{u}| + \frac{Q_m}{\epsilon_p^2}) \mathbf{u} + \mathbf{F} \right) \quad \text{(Equation 13)}$$

$$\nabla \cdot (\rho\mathbf{u}) = Q_m$$

In these equations:

μ is the dynamic viscosity of the fluid in (kg/(m·s))

\mathbf{u} is the velocity vector in (m/s)

ρ is the density of the fluid (kg/m³)

p is the pressure in (Pa)

ϵ_p is the porosity

κ is the permeability tensor of the porous medium in (m²)

Q_m (SI unit: kg/(m³·s)) is a mass source or mass sink

\mathbf{F} is force term which can represent the influence of gravity and other volume forces in (kg/(m²·s²))

The Brinkman equations is applied to the channel and GDL domains under steady state conditions, and therefore no time-dependent terms are involved in the equations. The walls of channel are considered in “No Slip” condition which indicates that the velocity of fluid is zero at the fluid-wall interface. On the other hand, the channel-GDL interface is under “Leaking Wall” condition, which is assumed to be simulating the porous GDL wall.

4.3.2 Transport of concentrated species

In COMSOL Multiphysics, the transport of concentrated species interface is responsible for diffusion driven mass transport. The formulation of equation differs depending on the mechanism of mass transport and the selected model of diffusion. In this study Mixture Averaged diffusion model is chosen since it is robust and not expensive computationally. Binary gas diffusivities from the aforementioned Fuller correlation (Equation 11) are used for the diffusion coefficient in Maxwell-Stefan built-in model. When the Maxwell-Stefan diffusion model is used, Equation 14 describes the relative mass flux vector:

$$\mathbf{j}_i = -\rho_g \mathbf{D}_i^{mk} \nabla \omega_i - \rho_g \mathbf{D}_i^{mk} \nabla \omega_i \frac{\nabla M_n}{\nabla M_n} - \frac{\mathbf{D}_i^T}{T} \nabla T \quad \text{(Equation 14)}$$

$$\mathbf{D}_i^m = \frac{1 - \omega_i}{\sum_{k \neq i} \frac{x_k}{\mathbf{D}_{ik}}}$$

Where D_i^{mk} is the multicomponent Fick diffusivities in m^2/s , ω_i is the mass fraction of species I, and D_i^T is the thermal diffusion coefficient in $(kg/(m \cdot s))$.

Since diffusivity is temperature dependent, it is the monitoring parameter to evaluate the effect of temperature on the yield of the desired reaction. The following table presents the binary gas diffusivities of the available species in the system at different temperatures:

Table 4: Binary gas diffusivities of the model species at different temperatures

Species	Binary diffusivity [m^2/s] @ 298 K	Binary diffusivity [m^2/s] @ 323 K	Binary diffusivity [m^2/s] @ 323 K
CO ₂ _CO	1.37×10^{-5}	1.86×10^{-5}	2.12×10^{-5}
H ₂ O_CO	2.59×10^{-5}	2.98×10^{-5}	3.39×10^{-5}
CO ₂ _H ₂ O	2.10×10^{-5}	2.43×10^{-5}	2.77×10^{-5}

4.3.3 Electrode Surface Coupling

The “Electrode Surface Coupling” physics are used to couple the chemical flux of species to the electric current density. In this case, the electrochemistry interface of COMSOL defines the reaction stoichiometry. In the chemical species transport interfaces, manual coupling is done, and it considers the current density as the driving force of the reaction (or rate of reaction). Porous Electrode Coupling node is the assigned coupling node to simulate the porous gas diffusion electrodes.

This node is used to describe a flux boundary condition in an Electrochemistry interface based on current densities of one or more Electrode Reaction nodes. According to Faraday's law, the flux is directly related to the current densities and stoichiometric coefficients, as described by Equation 15.

$$N_j = \frac{v_{jm} i_m}{n_m F} \quad \text{(Equation 15)}$$

This means that the flux N_j of chemical species j into the surface is proportional to the current density i_m due to reaction m drawn at the catalyst layer. The constant of proportionality is the stoichiometric number for the species divided by n , the number of electrons transferred per mole of reactant, in a reductive direction and F the Faraday constant (96485 C/mol, the absolute charge on a mole of electrons).

In this way, it is possible to couple the local flux of chemical species to the applied current density, using the stoichiometry of the electrochemical reaction involved in the model. If multiple reactions are involved at the electrode, the sum of the current density contributions is typically considered. However, in this model only the main CO₂ reduction reaction is taken into account for simplicity.

5. Results and discussions

This chapter presents the results of the experimental work of this research, followed by the results of the theoretical model developed for the gas flow channel. The experimental results will include the results of chronopotentiometry runs, mass flow meter (MFM), faradaic efficiencies (FE).

5.1 Experimental results

5.1.1 Chronopotentiometry

According to the plan of experiments discussed in Chapter 3, the performance of the electrochemical cell is tested in terms of selectivity or faradaic efficiency (FE) for the main products of CO₂RR on silver catalyst: CO and H₂. A total of 20 GDE samples were tested using chronopotentiometry experiments, in which constant current is applied to the working electrode for a period of one hour. The cell potential is monitored in the potentiostat over the entire period of the experiment, as can be seen in Figure 21. The figure represents a sample of chronopotentiometry tests performed at of 30 sccm inlet flow rate. As shown in the graphs, the cell potentials over time follow a similar trend for all of the current densities applied. It is clear that the voltage increases more negatively with time until it stabilizes after few minutes. Although the GC takes injection samples every five minutes from the start of experiment, only the injections taken at a stable cell potential are considered in calculating FE of the products. Small continuous fluctuations in the potential versus time plot are attributed to the formation of bubbles at the active surface of electrode during the electrochemical reaction. Also, the stability of potential curve is an indication that the cell works properly in reducing CO₂ at the given operating conditions. All of the completed experiments in this work show similar curves with different cell potentials depending on the applied current and inlet flow rate.

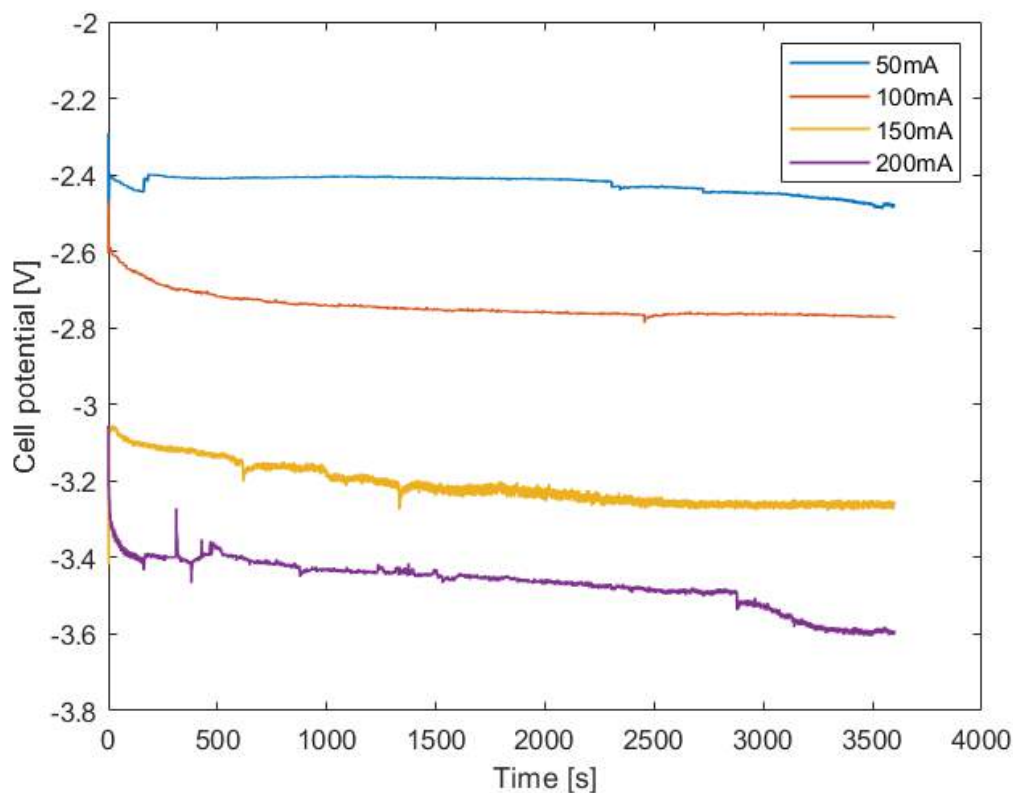


Figure 21: Chronopotentiometry tests at fixed flow rate 30sccm; and variable current densities

Another important observation from Figure 21 is the frequent oscillations in the cell voltage at high current densities (150-200 mA/cm²). The negative voltage shifts to more negative values towards the end of the experiments at 200 mA/cm², which is attributed to the higher resistances that system needs to overcome at elevated current densities. These challenges are further discussed in the results of MFM and FE in the coming sections. The average cell potentials of all the experiments can be found in Appendix C.

5.1.2 Mass flow meter (MFM)

The continuous observation of the outlet flow rate throughout the duration of experiments is very critical in order to ensure obtaining reliable results. Therefore, reliability tests are performed to the MFM prior to performing any electrochemical experiments. This is done by flowing CO₂ directly to the MFM, without passing it to the cell or any other compartment (humidifier, trap...etc), to check if the outlet flow rate of MFM matches the inlet flow rate. For most of the experiments, the MFM reading did not match the inlet flow rate during the reliability test. This could be attributed to salt accumulation at the connections of the MFM, which is expected to partially block the flow of CO₂, and subsequently gives lower outlet flow rates at the MFM. After consulting the lab technicians, it was understood that the issue would not be resolved within the time frame of this research. Therefore, a correction factor was introduced to the inaccurate MFM data based on multiple reliability tests before every day of experiments.

Figure 22 presents a compilation of MFM data of outlet flow rates for complete one-hour experiments at $100\text{mA}/\text{cm}^2$ at different inlet flow rates. The MFM data for the remaining experiments can be found in the appendices. The flow rate starts building up when all components are connected and before running the potentiostat. Once the flow rate stabilizes, the electrical current is applied, and the electrochemical reactions occur in the cell. It is important to note that the aforementioned reliability test (direct MFC-MFM connection) was performed earlier on the day of experiment, and it has shown that 30 sccm inlet flow rate, for instance, was equivalent to an MFM reading of around 24 sccm. After connecting the cell and the external compartments to the MFM, it can be seen in Figure 22 that the outlet flow rate is stabilized slightly below 24 sccm, which represents a “green light” to run the potentiostat and apply the desired current. Once the current is applied, a significant drop in outlet flow rate is observed as the electrochemical reactions take place and the CO_2 start being consumed. Since the GC takes injection samples every five minutes for one-hour experiment, twelve spikes of MFM curve can be seen at the time of each GC injection.

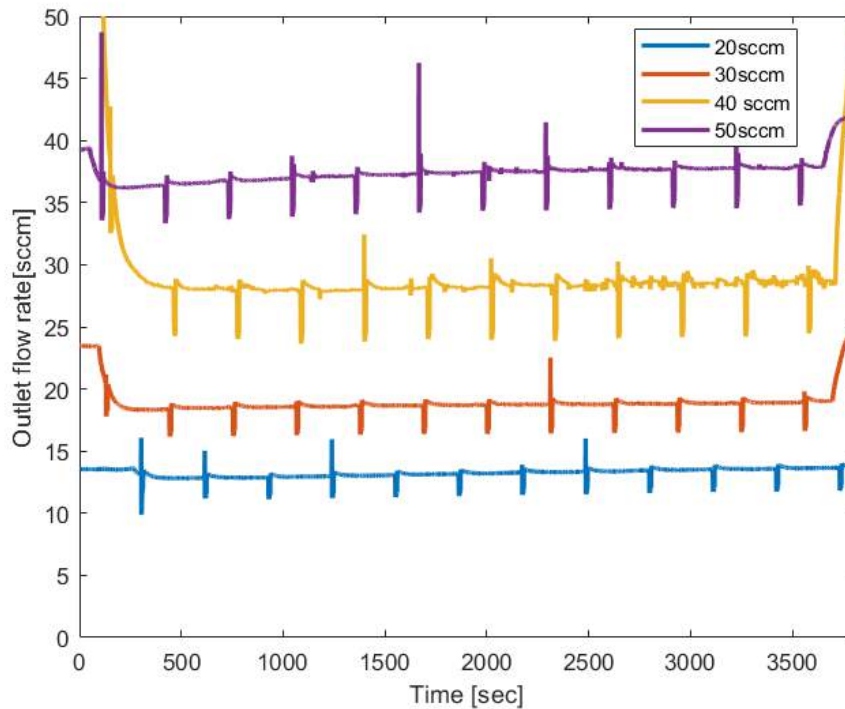


Figure 22: Plots of the outlet mass flow rate over the time of experiments at fixed current density of $100\text{ mA}/\text{cm}^2$ and variable inlet flow rate.

The MFM behavior shown in Figure 22 was consistent for current densities of 50, 100 and $150\text{ mA}/\text{cm}^2$ as can be observed in the plots of average outlet mass flow rates in Appendix A. On the other hand, when $200\text{ mA}/\text{cm}^2$ was applied, the behavior was similar only at low flow rate (20 sccm), as presented in Figure 23. It can already be observed that although the behavior seems to be stable at 20 sccm, the outlet flow rate shows relatively larger fluctuations (noise) at the last couple of injections at the end of experiment as seen in Appendix A. It is understood that this

instability in the flow rate curve at $200\text{mA}/\text{cm}^2$ is associated with accumulation of potassium carbonate (K_2CO_3) or potassium bicarbonate (KHCO_3) at the back side of GDL, which forms obstacles inside the gas flow channel and active catalyst sites. The precipitation of these salts is a common issue for CO_2 electrolyzers in MEA configuration when using anion exchange membranes and concentrated KOH solution as anolyte [63].

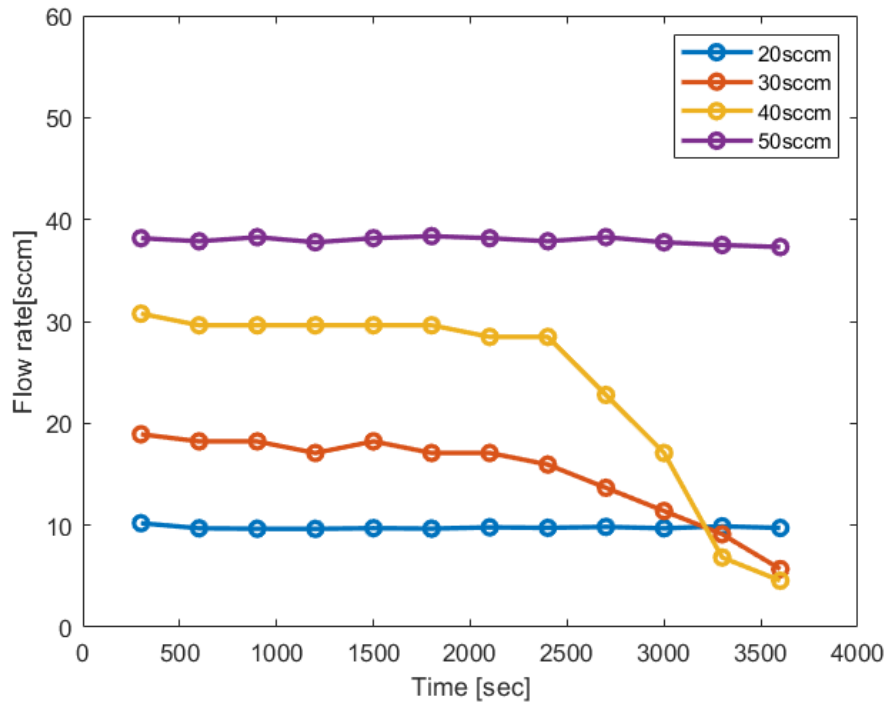


Figure 23: Plot of the average outlet mass flow rate after each GC injection; at fixed current density of $200\text{mA}/\text{cm}^2$ and variable inlet flow rates

Using the same current density ($200\text{mA}/\text{cm}^2$) with higher flow rate (30-40sccm) lead to a drastic decrease in the performance of the cell. The comparison of MFM data between different inlet flow rates at $200\text{mA}/\text{cm}^2$ indicates a significant drop in the cell performance at 30 and 40 sccm. At 50 sccm, it is believed that there was an experimental error, as we did not see the expected drop in flow rates. Figure 23 shows that when 30-40 sccm of CO_2 is supplied at $200\text{mA}/\text{cm}^2$, the outlet flow rate is not stable after around 40 minutes of operation. The flow rate gradually drops to reach as low as 5 sccm at the last GC injection. Looking at the gas flow channel after the experiment (Figure 24), large white crystals can be observed blocking the flow channel. This can justify the irregular behavior of the MFM curve and the very low cathodic outlet flow rate towards the end of experiment (Figure 23).



Figure 24: Picture of the cathode-side gas flow channel after conducting CO₂RR experiment at 200mA/cm² and 40 sccm. Large salt crystals are clearly visible

By comparing the backside of GDL after experiments, as depicted in Figure 25, it is clear that more salts are precipitated on the GDL that was used at higher inlet flow rate (Figure 25B) in comparison to the GDL used at lower flow rate (Figure 25A). This can be attributed to the high amount of CO₂ that is neutralized at the cathode due to the alkalinity of the environment. The produced carbonate/bicarbonate will react with migrated K⁺ ions at the cathode to form precipitated salt. The carbonate/bicarbonate can also transport through the membrane to the anolyte solution where they will either react with K⁺ to form dissolved/precipitated potassium salts or react with H⁺ to release CO₂ at the anode side. This means that a significant amount of the inlet gas flow is lost before reaching the cathodic outlet and MFM.

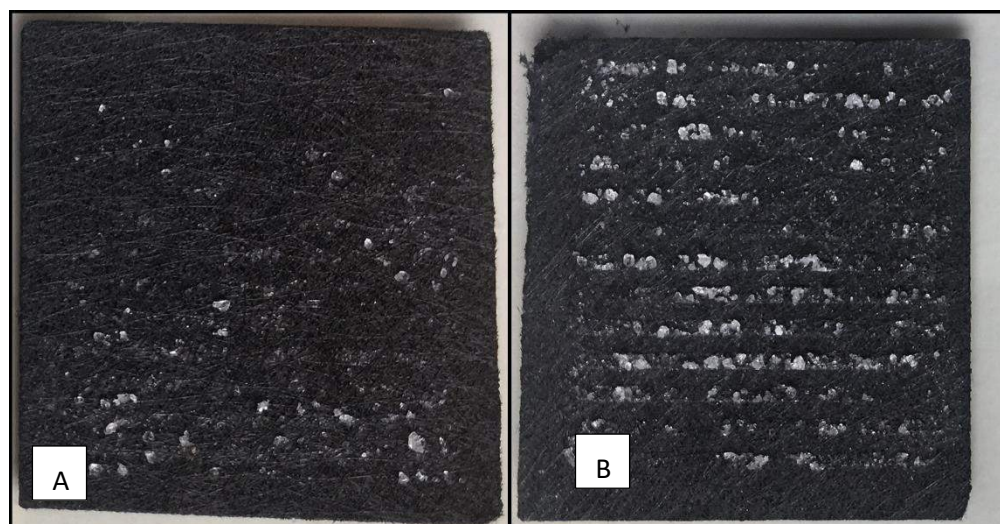


Figure 25: Pictures of the back side of the GDL after conducting CO₂RR experiments at 200mA/cm² and different inlet flow rates. A) at 20 sccm, B) at 40 sccm

It should be pointed out that since the system was not able to perform a stable complete 1-hour experiments at $200\text{mA}/\text{cm}^2$, the initial plan of applying a current density of $300\text{mA}/\text{cm}^2$ was cancelled. It is expected to see even more salt precipitated at the cathodic flow channel, which would result in a worse overall performance of the cell.

To show the relation between outlet flow rate and the total current densities, the loss in flow rate is plotted against the current density, as demonstrated in Figure 26. The flow rate loss in this case is calculated as (Loss = inlet flow rate of CO_2 – average outlet flow rate – average H_2 flow rate). The flow rates of H_2 are determined using the FE of H_2 produced during the experiment, which is discussed in the following section: **5.1.3 Faradaic efficiency (FE)**. The flow rate loss can also be assumed as the amount of CO_2 that crossed over the membrane to the anode side.

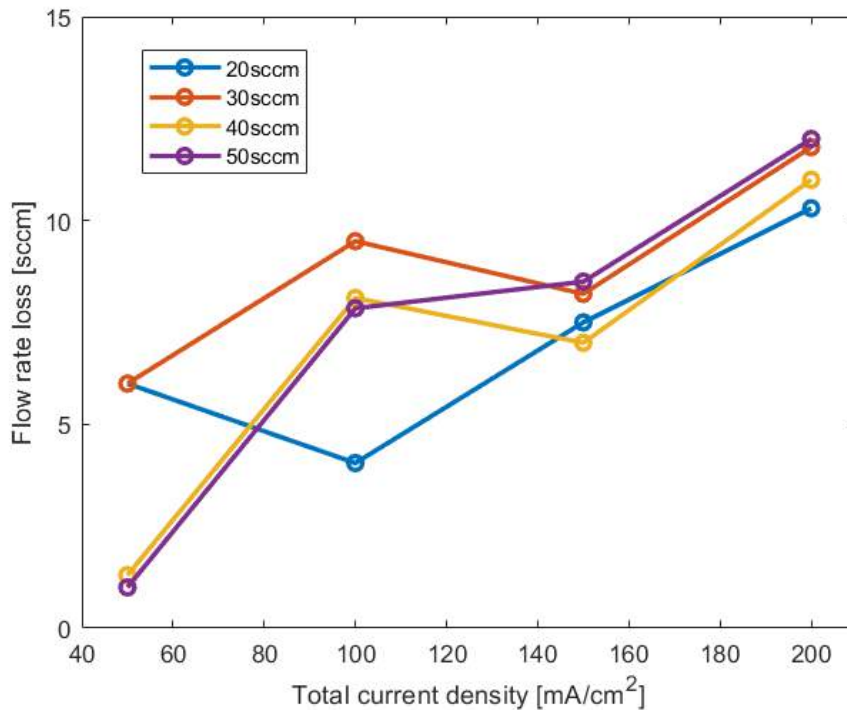


Figure 26: Flow rate loss over total current densities at different inlet flow rates.

From the available experimental data, it is understood that the effects of salt precipitation and CO_2 cross over are more noticeable at higher current densities with higher flow rates. It is believed that water migration and flooding of the cathode promote the CO_2 crossover to the anode which affects both outlet flow rates and selectivity at higher current densities. The effect on selectivity can also be seen in the following section.

Although some of the data in Figure 26 show do not go in accordance with the expected trend (e.g., relatively high losses at 30sccm), it is expected that these random results occur due to experimental error. It is recommended to repeat the experiments to increase the reliability of the results.

5.1.3 Faradaic efficiency (FE)

The gas phase products are analyzed by the GC simultaneous to the chronopotentiometry measurements to identify and quantify the products. The GC takes a sample injection of the cathodic outlet stream every five minutes for one hour. In total, 12 injections are analyzed for each experiment, and the calculation of FE is done for each injection separately. Figure 27 presents an example of the FE results for one of the conducted experiments at a total current density of 50 mA/cm² and inlet CO₂ flow rate of 20 sccm. In order to obtain consistent and reliable results, it is important to check the potentiostat data of the chronopotentiometry test to determine the period of stable cell voltage. Although the experiment is run for one hour, the FE is averaged over the period of constant cell potential.

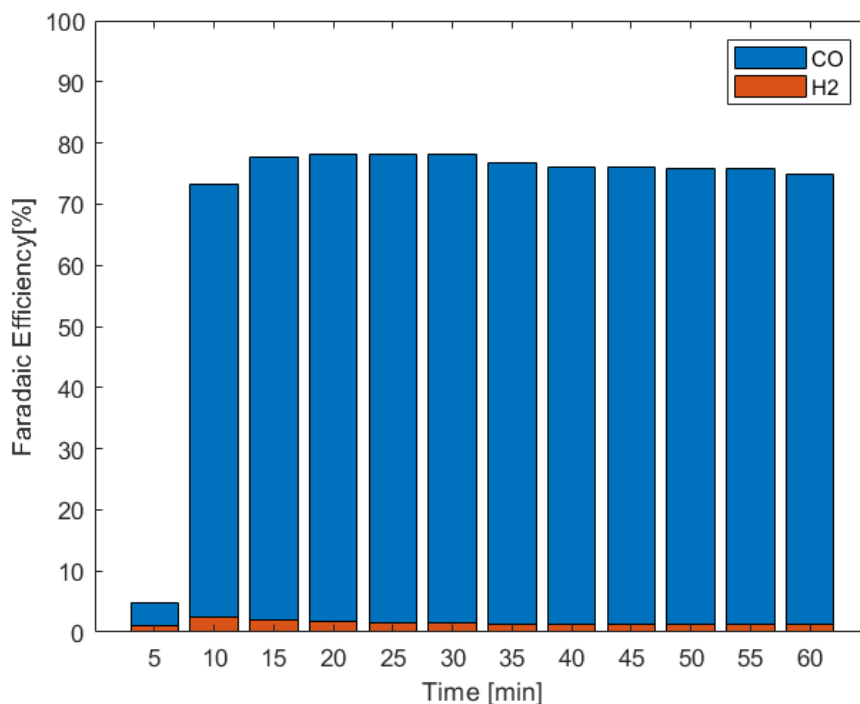


Figure 27: Faradaic efficiency of the gas products of CO₂RR on Ag at 50 mA/cm² and 20 sccm

Since only CO and H₂ are observed during GC operation, it is expected that the current applied to the cell would contribute to producing either CO or H₂ only. However, the FE calculations have shown that the sum of FEs for CO and H₂ was significantly lower than 100% for all the experiments. It is expected that the “lost” electrons are attributed to CO₂ reduction to produce formate, which gets oxidized again to CO₂ on the anode side [64]. This is considered an undesirable side reaction for CO₂RR on Ag catalyst in an AEM-based MEA, because energy (electrons) is consumed to produce (and decompose) a product that cannot be recovered. It is important to note that this result requires post-reaction analysis of the anolyte solution (e.g., HPLC) to become conclusive.

Figure 28 presents the FE for CO and H₂ over total current density in all the completed experiments in this research. It can be clearly seen that running the cell at relatively high current densities resulted in the loss of selectivity towards CO production. This can be attributed to the

increased rate of cathode flooding at high current densities, as predicted by Brushett et al [65]. The FE of CO dropped to as low as 48% at 200 mA/cm² and 30 sccm. This denotes that only around half of the current supplied is actually contributing to the formation of the desired product. The low CO₂ conversion at these conditions (200 mA/cm² and 30 sccm) is also supported by the observation of frequent oscillations of the cell voltage over time from the chronopotentiometry plot, shown in Figure 21 at 200 mA/cm².

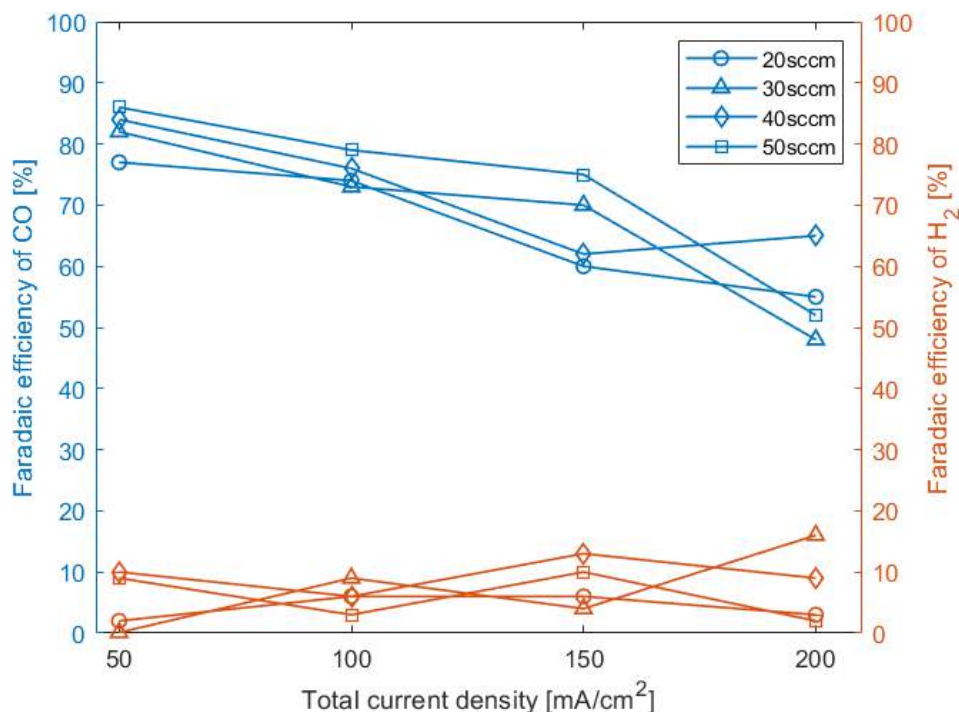


Figure 28: FE for CO and H₂ production over total current density at different inlet flow rates

As mentioned earlier, the GC was able to detect H₂ in the cathodic outlet stream, which is produced electrochemically at the cathode through HER (explained in theory section, Chapter 2). Figure 28 gives an overview of the H₂ selectivity over total current density in all completed experiments. Based on the figure, it is hard to make a correlation between FE of H₂ and the current density or inlet flow rate. The trend seems to be random which makes it difficult to draw any conclusion. For instance, the lowest FE of H₂ recorded was at 50 mA/cm², while the second highest FE of H₂ was also obtained at 50 mA/cm². Ideally, it would be suggested to repeat all of the experiments, but that was not possible due to the limitation of lab access. In general, it is expected that H₂ production would increase as the current density increases, coupled with the collapse of CO production.

It is notable that there is a relation between the FE for H₂ and FE for CO at high current density experiments performed in this work. Looking at Figure 29, which presents the FE's resulted after running one of the samples at 200 mA/cm² and 40 sccm, it is observed that the CO₂ conversion to CO is degraded after a certain point of time and the HER becomes more dominant, especially at

the last GC injections. All the experiments conducted at 200 mA/cm^2 have shown a similar trend, as seen in the appendix A. This observation comes in a good agreement with the experimental results of the past work of Larrazabal et al [64]. The analysis of Larrazabal et al claims that the loss of selectivity towards CO formation at high current densities is likely a result of mass transfer limitations caused by water migration and flooding of the cathode. This is a common issue for MEA setup with a liquid-fed anode. Once the electrode is flooded, the diffusion length for CO_2 to the catalyst layer increases to the point where CO_2 flux is not sufficient to match the current demand to produce CO. The HER becomes favorable throughout the wetted parts of the cathode [65]. It is also worth mentioning that these periods of HER dominance occurred simultaneous to a substantial increase in the negative cell voltage which could possibly be attributed to flooding of GDE cathode of such an exchange-MEA [44].

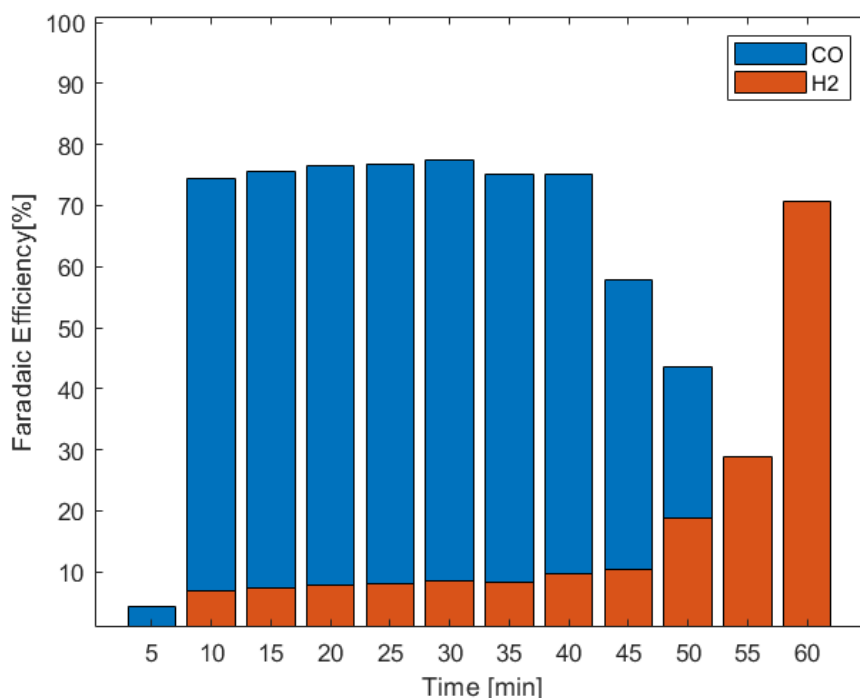


Figure 29: FE of the gas products of CO_2RR on Ag sample at 200 mA/cm^2 and 40 sccm .

It was previously shown that the sum of FE's for CO and H_2 is significantly lower than 100% due to loss of electrons towards other products such as HCOO^- , especially at elevated current densities. Figure 30 presents an overview of the faradaic loss over total current density for all of the samples tested. The faradaic loss in this case represents the percentage of applied current that do not contribute to either CO or H_2 production. The figure shows relatively high FE losses in general for CO_2RR on Ag using KOH exchange MEA. It is also observed from the figure that the FE loss increases with total current density and is inversely related to inlet flow rate. Moreover, it is reported by the works of Weber et al [44], and Larrazabal et al [64], that a substantial fraction of CO_2 is lost to the anode as formate (HCOO^-) at total current densities higher than 200 mA/cm^2 . Subsequently, a considerable fraction of the current does not contribute to the formation of the main gas phase products (CO and H_2).

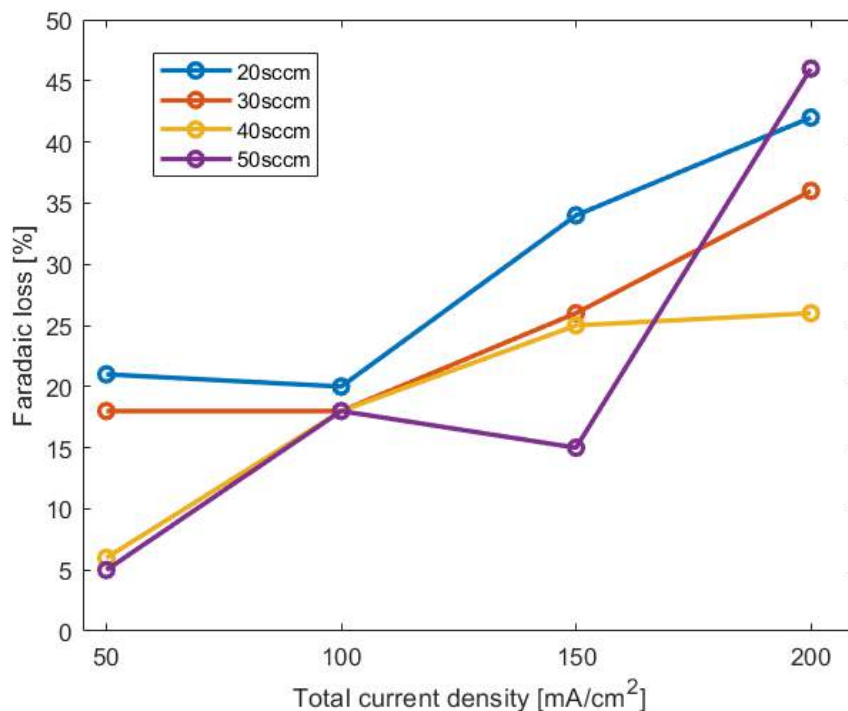


Figure 30: FE loss over total current densities at different inlet flow rates

According to Sinton et al, it is suggested that a very high local pH at the reaction interface promotes the CO₂ reduction to HCOO⁻ at the expense of production of CO. This is likely to occur at high cathodic overpotentials needed to achieve high current densities, due to the rapid proton consumption and water splitting [39]. Reducing the concentration of the anolyte solution while analyzing the solution post reaction would be a helpful step to understand the effect of the local pH. It is recommended to test the cell under the same conditions using new anolyte solution with lower KOH concentration.

5.1.4 Performance Challenges

There are several possible techniques in order to make more conclusive results of FE and product concentrations. Using high-performance liquid chromatography (HPLC) to the liquid anolyte solution post-reaction would be useful to detect the products formed through CO₂ cross over and gain a better understanding on the FE losses. Another possibility would be measuring the pH of the anolyte solution after each experiment, which would give an interesting insight on the effect of current densities and flow rates on the alkalinity of the anolyte, and how would that affect the selectivity of the desired products.

An additional challenge to be addressed is the precipitation of crystalline potassium salts on the cathodic flow channel. Since it is a common issue for KOH exchange MEA cells and AEM, there are multiple solutions reported in literature to overcome this challenge. One of the reported solutions is using pure deionized water as the electrolyte (anolyte) instead of strong alkaline

solutions [44] . However, the alkalinity of anolyte solution is essential to favour CO₂ reduction over HER as explained previously in this report. Thus, decreasing the concentration of KOH in the anolyte solution could possibly help reducing the levels of salt precipitation at high current densities. It was not possible to test different anolyte concentrations in this work due to the limited time frame of project.

Furthermore, it was reported that increasing the temperature of the humidified CO₂ inlet was a useful approach to mitigate the salt formation. The theory behind this approach is to supply more water vapor into the reactor while also increase the solubility of carbonates/bicarbonates, and thereby avoid the accumulation of these carbonates in the gas flow channel. On the other hand, it was reported by Janaky et al that increasing the water content of the inlet resulted in a smaller FE for CO and a higher FE for H₂, in comparison to low temperature tests. This is due to the fact that the increased amount of water in the cell improves the probability of HER. Also, flushing the cell periodically with liquid water has been an effective method to periodically wash the carbonate/bicarbonate salts before larger plaque would accumulate. This method could help solving the issue of salt formation without heavily compromising the performance of the cell [63].

5.2 Model Results

The objective of the modelling work in this research was to gain better understanding of the CO₂ consumption along the gas flow channel. The developed 2D model in COMSOL Multiphysics is capable of giving quick estimates of reactant and product concentration of an ideal plug flow scenario.

5.2.1 Model validation

The accuracy of any finite element method model is directly related to the finite element mesh that is used. The function of the mesh is to subdivide the geometry into smaller domains (elements). As the size of these elements is decreased, as the mesh is refined, and the computed solution will approach the true solution for the equations being solved. It is essential, however, to consider the limitation of finite computational resources and time. Therefore, the objective is to minimize the error between the exact and computed solution, and to find the mesh size that gives a trade-off between the computation time and solution accuracy. To validate the model, the simulation is run at different mesh sizes while monitoring the parameter of interest. In this case, the molar concentration of CO₂ at the outlet of the channel is monitored during the simulation.

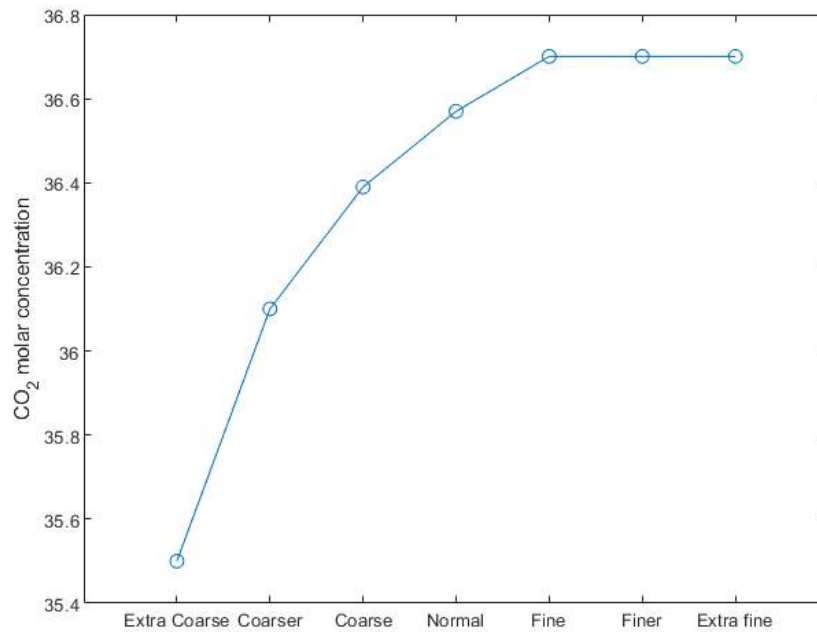


Figure 31: The mesh independence study for model validation, monitoring the molar concentration of CO₂ near the outlet of the channel; Current density: 100mA/cm², inlet flow rate: 30sccm

The results in Figure 31 present the change of the computed solution with the refinement of the mesh. By tracking the output parameter (CO₂ molar concentration) as the mesh size is varied, it is possible to evaluate whether the converged solution is independent from the number of elements. It can be seen in Figure 31 that the value of CO₂ molar concentration slightly increases as the mesh is further refined, which represents an enhancement of the solution accuracy. It is also observed that after using Fine mesh, there is no clear difference in the solution output. Although using Finer and Extra Fine meshes provide a solution that is converged and accurate, it comes with computational and time costs. Table 5 presents the details of the different mesh sizes which have been used in order to perform the mesh independence study of the model. Fine mesh is capable of converging the same solution as Finer and Extra Fine, while using less elements and shorter simulation time.

Table 5: Mesh Details

Parameter	Extra Coarse	Coarser	Coarse	Normal	Fine	Finer	Extra Fine
Number of elements	2925	5756	9310	18870	32371	50161	226907
Computational time	1.5 min	2 min	4 min	8 min	14 min	25 min	2h 28min

Therefore, Fine mesh is selected for the analysis of the results of this model.

5.2.2 Parametric Analysis

The main parameters which were tested during the experimental work are the total current density and the inlet flow rate of CO₂. These parameters are also varied in the COMSOL model to compare the conversion profiles along the flow channel. A parametric sweep was performed in COMSOL Multiphysics, which is an iterative process in which simulations are repeatedly run using different values of current density and inlet mass flow rate. Table 6 reviews the range of values used for the parametric sweep analysis.

Table 6 : Parametric Sweep values

Manipulated Parameter	Parameter value list	Unit
Current Density	[50, 100, 150, 200, 300]	mA/cm ²
Inlet flow rate	[10, 20, 30, 40]	sccm

The values were selected to be matching the planned experiments initially so that we can compare and validate the results. However, replicating the real process was not possible in this simulation, as clarified in the Model Description section. Based on the simulation, the results of CO₂ conversion rate along the width of the cathode at constant current density can be seen in Figure 32 and Figure 33. The figures present the effect of flow rate on mole fractions of both species (CO₂ and CO) as they diffuse through the porous GDL at the center of the cathode. It is obvious in Figure 32 that the mole fractions of CO₂ decrease as we go from the backside of the channel towards the catalyst layer. This occurs since the catalyst layer is where the reaction takes place, and the CO₂ gets converted to CO.

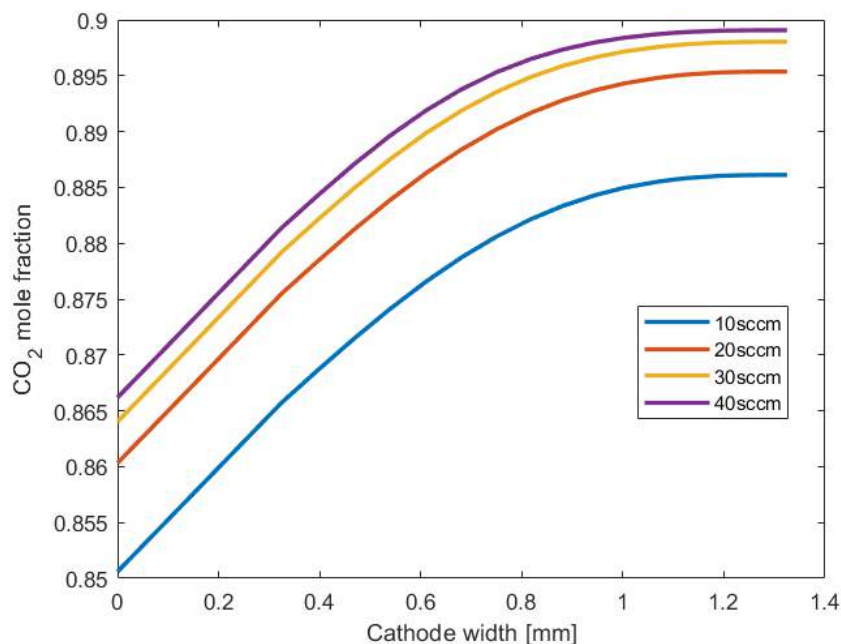


Figure 32: Mole fraction of CO₂ along the width of cathode at a fixed current density (300 mA/cm²) and four different inlet flow rates. The x axis starts from the catalyst layer @ x=0, and ends at the backside of the flow channel @ x=1.325

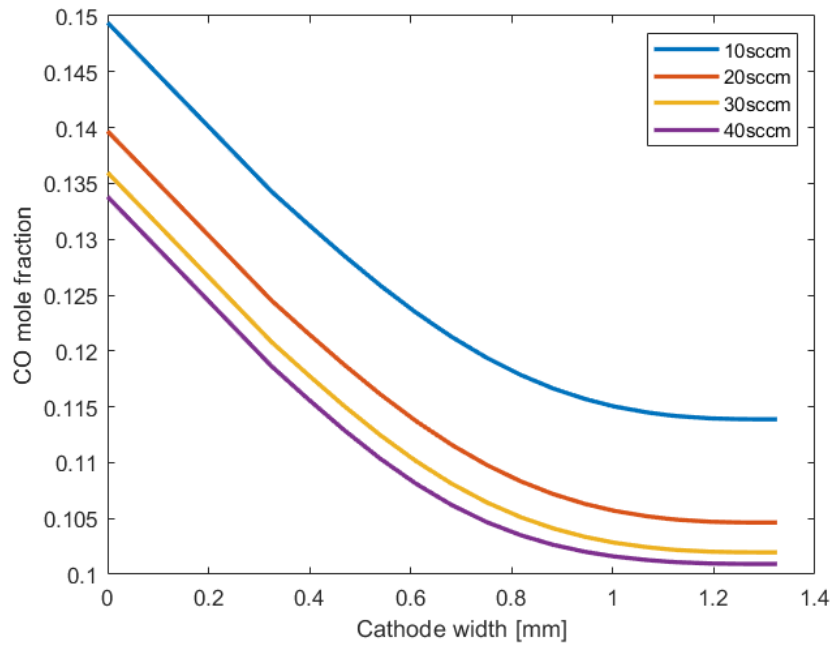


Figure 33: Mole fraction of CO along the width of cathode at fixed current density $300\text{mA}/\text{cm}^2$. The x axis starts from the catalyst layer @ $x=0$, and ends at the backside of the flow channel @ $x=1.325$

It can be observed that at fixed current densities, the inlet flow rate is inversely proportional to the mole fraction of the produced CO. This suggests that as we increase the flow rate, less percentage of the inlet gas stream is actually converted. Thus, in order to achieve high conversion at high CO_2 flow rates, high reaction rates are needed. In this scenario, reaction rates are equivalent to the total current densities, as it is defined by the Electrode Surface Coupling node of the simulation. Figure 34 presents the effect of reaction rates (current densities) on the mole fraction of CO_2 in the channel. As expected, higher current densities resulted in lower CO_2 mole fractions, indicating that CO_2 is getting consumed at higher rates.

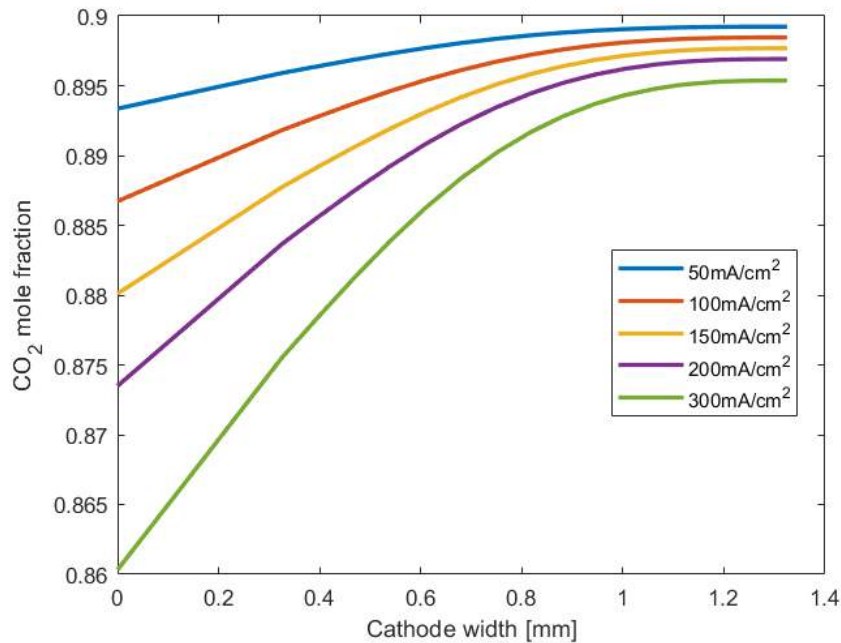


Figure 34: Mole fraction of CO₂ along the width of cathode at fixed flow rate 20sccm. The x axis starts from the catalyst layer @ x=0, and ends at the backside of the flow channel @x=1.325

It is important to clarify that the initial idea of the parametric analysis was to use the results of conversion profiles along the flow channel to identify the optimal conditions for the cell performance. Due to the simplification and assumptions of the model, it turned out to show an ideal-scenario results which do not represent the real electrochemical process.

5.2.3 Temperature Influence on Cell Performance

The temperature dependent performance and efficiency of the cell has been studied to determine the optimal operation temperature of the theoretical model. This was done by monitoring the molar concentration of species in the channel at three different temperatures (298K,323K,348K) while keeping the inlet flow rates and current densities constant. Figure 35 and Figure 36 present the molar concentration profiles of CO₂ and CO respectively, along the width of the cathode. The molar concentrations of CO₂ gradually decrease as it reaches the catalyst surface, following an identical trend for all temperatures, as shown in Figure 35. On the other hand, the molar concentrations of CO considerably increase, in an identical profile, as more CO is formed near the catalyst layer.

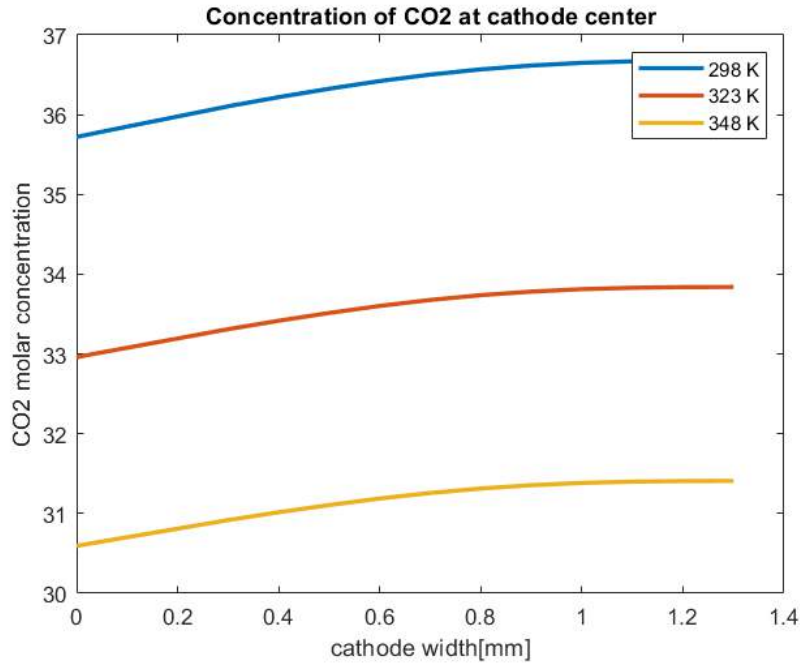


Figure 35: Molar concentration of CO₂ along the width of cathode at different operation temperatures. The x axis starts from the catalyst layer @ x=0, and ends at the backside of the flow channel @x=1.325

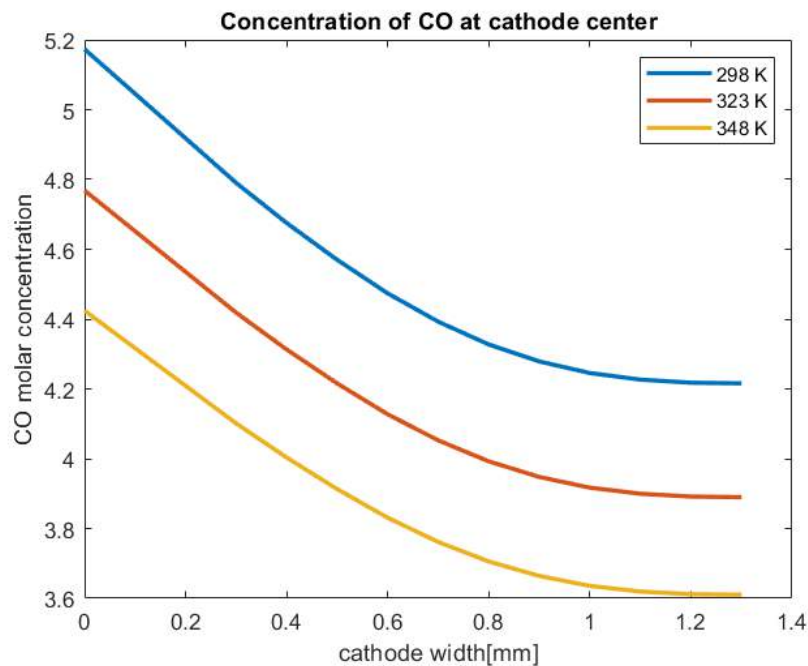


Figure 36: Molar concentration of CO along the width of cathode at different operation temperatures. The x axis starts from the catalyst layer @ x=0, and ends at the backside of the flow channel @x=1.325

Additionally, it is seen that the molar concentrations of both species drop as the operation temperature increases from 298K to 348K. This can be attributed to the limitations of the model, as it only considers the diffusivities of species without involving reaction kinetics. The temperature elevation is expected to have a negative effect on the FE for CO, as it would impact the catalytic selectivity between the CO₂RR and HER. Clearly, the Ag cathode favors the CO₂RR over HER, which entails that the activation energy of the HER is greater than that of the CO₂RR. Increasing the operation temperature benefits the reaction with greater activation energy. [66]

However, this does not describe the scenario in Figure 36 since the HER is not modelled in the simulation. The model assumes ideal gas behavior, implying an inverse proportion between species concentration and operation temperature, neglecting the kinetic effects. Therefore, it is difficult to make a conclusive statement on the temperature influence with the limited results of the model. It is understood that the implementation of current distribution in COMSOL and incorporating the electrochemical reaction kinetics would make the model more realistic, but the complexity of these steps go beyond the scope of this project.

6. Conclusions and Recommendations

6.1 Conclusions

In this research, the electrochemical reduction of CO₂ to CO has been investigated on Ag catalyst using KOH-exchange MEA reactor. Chronopotentiometry experiments were performed to evaluate the influence of current densities and inlet flow rates on the CO selectivity. Also, the effects of mass transport and operating temperature of the MEA have been researched by developing a 2D model in COMSOL Multiphysics for the cathodic gas flow channel.

The experimental setup was capable of reducing CO₂ to CO at high current densities (up to 200 mA/cm²). However, the system experienced significant losses in the selectivity for CO as the current density increased. Also, drastic drops in the outlet gas flow rate were observed during the operation at to 200 mA/cm² which are attributed to the precipitation of potassium salt blocking the gas flow. This presents a challenge for the performance of KOH-exchange MEA cell at industrially relevant current densities. On top of that, the FE loss was relatively high, when compared to the literature, in all of the experiments performed, considerable fractions of the applied current do not contribute to neither CO₂ reduction nor H₂ evolution. It is expected that the “lost current” goes into formate production, which crosses the membrane to the anode and gets oxidized “lost”. Although this observation was reported in multiple sources in literature, the analysis of anolyte solution would have provided more conclusive results to justify the high losses.

In the computational work of this research, it was possible to develop a working model representing a gas flow channel with porous GDL on top of it. The model represented a simplified plug flow reactor in porous media. When evaluating the influence of the same process parameters which were tested experimentally, it was found that the increase of inlet flow rate results in lower fractions of products. On the other hand, the current densities were considered as reaction rates and consequently resulted in higher conversions. Moreover, the cell temperature effect on the concentration profile was also tested on the basis of species diffusivity. However, this approach did not produce reasonable results, as the reaction kinetics were not incorporated in the simulation.

Although the model successfully managed to generate quick estimates of the molar concentration along the flow channel, the results in general represent an ideal situation which does not replicate the complexities of the real electrochemical CO₂ reduction.

6.2 Recommendations

Both the experimental and modelling work of this research have had areas for improvement in order to obtain more conclusive results. Due to the limited lab access throughout the timeframe of this project, it was not possible to repeat the experiments to check if the results are reproducible. It is also to do another set of the same experiments using diluted anolyte solution which is expected to reduce the crossover of K⁺ ions and thereby minimize the accumulation of salts at the cathode. Also, it is advised for future work to give more attention to analyzing the anolyte solution post-reaction. This can be by easily checking the pH of solution after each experiment, which could give an indication of CO₂ crossover to the anode side. Another technique would be performing High Performance Liquid Chromatography (HPLC) to identify and quantify the dissolved components.

Regarding the modelling work, it is recommended to incorporate the full electrochemistry physics of COMSOL. Considering the high complexities of the process, it would be ideal if it is done as an entire research project separately, rather than a side-task.

7. Bibliography

- [1] AOAN, "Global Monitoring Laboratory - Carbon Cycle Greenhouse Gases," US Department of Commerce, NOAA, Global Monitoring Laboratory, [Online]. Available: <https://gml.noaa.gov/ccgg/trends/>.
- [2] S. K. a. P. K. Muhuri, "A novel GDP prediction technique based on transfer learning using CO2 emission datasets," *Appl. Energy*, vol. 253, p. 113476, 2019.
- [3] S. P. Socolow, "Stabilization Wedges: Solving the Climate Problem for the Next 50 Years with Current Technologies," [Online]. Available: <http://science.sciencemag.org/>. [Accessed 17 8 2020].
- [4] P. Taylor, "Energy technology perspectives 2010-scenarios and strategies to 2050," International Energy Agency, Paris, 2010.
- [5] C. E. Tornow, M. R. Thorson, S. Ma, A. A. Gewirth and P. J. and Kenis, "Nitrogen-based catalysts for the electrochemical reduction of CO2 to CO.," *Journal of the American Chemical Society*, vol. 134, pp. 19520-19523, 2012.
- [6] B. Rosen, "Ionic liquid-mediated selective conversion of CO2 to CO at low overpotentials," *Science*, vol. 334, pp. 643–644,, 2011.
- [7] Y. Hori, H. Wakebe, T. Tsukamoto and O. Koga, "Electrocatalytic process of CO selectivity," *Electrochim. Acta*, Vols. 39,, p. 1833–1839, 1994.
- [8] J. Qu, X. Zhang and Y. a. X. C. Wang, "Electrochemical reduction of CO2 on RuO2/TiO 2 nanotubes composite modified Pt electrode," *Electrochim. Acta*, vol. 50, no. 16-17, p. 3576–3580, 2005.
- [9] C. L. Ronald, "High Rate Gas Phase Reduction to Ethylene and Methane Using Gas Diffusion Electrodes," *Journal of The Electrochemical Society*, vol. 137, no. 2, 1990.
- [10] S. Verma, S. Lu and P. Kenis, "Co-electrolysis of CO2 and glycerol as a pathway to carbon chemicals with improved technoconomics due to low electricity consumption," *Nat Energy*, vol. 4, p. 466–474, 2019.
- [11] S. Verma, B. Kim, H. R. M. Jhong, S. Ma and P. J. A. Kenis, "A gross-margin model for defining techno-economic benchmarks in the electroreduction of CO2," *ChemSusChem*, vol. 9, p. 1972–1979, 2016.
- [12] K. Hara and T. Sakata, "Large Current Density CO2 Reduction under High Pressure Using Gas Diffusion Electrodes," *Bulletin of the Chemical Society of Japan*, vol. 70, no. 3, pp. 571-576, 1997.
- [13] B. e. a. Kumar, "New trends in the development of heterogeneous catalysts for electrochemical CO2 reduction.," *Catalysis*, vol. 270, p. 19–30, 2016.
- [14] T. C. Y. H. J. & B. C. P. Li, "Electrolytic CO2 reduction in tandem with oxidative organic chemistry," *ACS central science*, vol. 3, no. 7, pp. 778-783, 2017.
- [15] B. P. Sullivan and K. K. a. H. Guard., *Electrochemical and Electrocatalytic Reactions of Carbon Dioxide*, Elsevier, 2012.
- [16] W. L. a. F. J. Matthew Jouny, "General Techno-Economic Analysis of CO2 Electrolysis Systems," *Industrial & Engineering Chemistry Research*, vol. 57 , no. (6), pp. 2165-2177, 2018 .

- [17] K. P. Kuhl, E. R. Cave, D. N. Abram and T. F. Jaramillo, "New insights into the electrochemical reduction of carbon dioxide on metallic copper surfaces," *Energy Environ. Sci.*, vol. 5 (5), p. 7050–7059, 2012.
- [18] H. T. C. E. A. D. K. J. J. T. Kuhl KP, " Electrocatalytic conversion of carbon dioxide to methane and methanol on transition metal surfaces," *Am Chem Soc.* , 2014 .
- [19] O. Hideshi, M. C. Figueiredo and M. T. Koper, "Competition between Hydrogen Evolution and Carbon Dioxide Reduction on Copper Electrodes in Mildly Acidic Media," *Langmuir*, vol. 33, no. 37, p. 9307–9313, 2017.
- [20] Y. K. Hori and S. Suzuki, *Chem. Lett.*, p. 1695, 1985.
- [21] J. Wu, "Incorporation of Nitrogen Defects for Efficient Reduction of CO₂ via Two-Electron Pathway on Three-Dimensional Graphene Foam," *Nano Lett.*, vol. 16, p. 466–470, 2016.
- [22] D.-M. Feng, Y.-P. Zhu and P. ., a. M.-Y. Chen, "Recent Advances in Transition-Metal-Mediated Electrocatalytic CO₂ Reduction: From Homogeneous to Heterogeneous Systems," *Catalysts*, vol. 7, p. 373, 2017.
- [23] M. Gattrell and N. Gupta, "A review of the aqueous electrochemical reduction of CO₂ to hydrocarbons at copper," *Journal of electroanalytical Chemistry*, vol. 1, pp. 1-19, 2006.
- [24] Q. & J. F. Lu, "Electrochemical CO₂ reduction: Electrocatalyst, reaction mechanism, and process engineering," *Nano Energy*, vol. 29, p. 439–456, 2016.
- [25] J.-P. Grote, A. R. Zeradjanin, C. Serhiy, S. Alan, B. Breitbach and A. a. M. K. .. Ludwig, "Screening of material libraries for electrochemical CO₂ reduction catalysts—Improving selectivity of Cu by mixing with Co," *Journal of catalysis*, vol. 343, pp. 248-256, 2016.
- [26] R. Kortlever, J. Shen, K. J. P. Schouten, F. Calle-Vallejo and M. T. M. Koper, "Catalysts and Reaction Pathways for the Electrochemical Reduction of Carbon Dioxide," *Phys. Chem. Lett*, vol. 6, p. 4073–4082, 2015.
- [27] J. Kari, J. P. Olsen, K. Jensen, S. F. Badino, R. M. Krogh, K. Borch and P. Westh, "Sabatier Principle for Interfacial (Heterogeneous) Enzyme Catalysis," *ACS Catalysis*, vol. 8, no. 12, pp. 11966-11972, 2018.
- [28] A. J. Medford, A. Vojvodic, J. S. Hummelshøj, J. Voss, F. A. Pedersen, F. Studt, T. Bligaard, A. Nilsson and J. K. Nørskov, "From the Sabatier principle to a predictive theory of transition-metal heterogeneous catalysis," *Journal of Catalysis*, vol. 328, pp. 36-42, 2015.
- [29] D. D. Zhu, J. L. Liu and S. Z. Qiao, "Recent Advances in Inorganic Heterogeneous Electrocatalysts for Reduction of Carbon Dioxide," *Adv. Mater*, vol. 28, p. 3423–3452, 2016.
- [30] D. T. Whipple, E. C. Finke and P. J. A. Kenis, "Microfluidic Reactor for the Electrochemical Reduction of Carbon Dioxide: The Effect of pH," *Electrochem. Solid State Letters*, vol. 13, p. B109–B111, 2010.
- [31] I. A. J. & I. A. Merino-Garcia, "Productivity and Selectivity of Gas-Phase CO₂ Electroreduction to Methane at Copper Nanoparticle-Based Electrodes," *Energy Technol.*, vol. 5, p. 922–928, 2017.
- [32] C. M. Gabardo, "Combined high alkalinity and pressurization enable efficient CO₂ electroreduction to CO," *Energy & Environmental Science*, vol. 11, p. 2531–2539, 2018.
- [33] C. & L. H. Oloman, "Electrochemical processing of carbon dioxide," *ChemSusChem*, pp. 385-391, 2008.

- [34] R. B. Kutz, Q. Chen, H. Yang, S. D. Sajjad, Z. Liu and I. R. Masel, "Sustainion imidazolium-functionalized polymers for carbon dioxide electrolysis," *Energy Technol.*, vol. 5, pp. 929-936, 2017.
- [35] D. A. Salvatore, "Electrolysis of Gaseous CO₂ to CO in a Flow Cell with a Bipolar Membrane," *ACS Energy Lett.*, p. 149–154, 2017.
- [36] C. M. Gabardo, "Continuous Carbon Dioxide Electroreduction to Concentrated Multicarbon Products Using a Membrane Electrode Assembly," *Joule*, vol. 3, pp. 2777-2791, 2019.
- [37] S. Garg, M. Li, A. Z. Weber, G. Lei, L. Liye, R. Victor and G. a. R. T. E. Wang, "Advances and challenges in electrochemical CO₂ reduction processes: an engineering and design perspective looking beyond new catalyst materials.," *Journal of Materials Chemistry*, vol. A 8, no. 4, pp. 1511-1544, 2020.
- [38] Y. C. Li, Z. Dekai, Y. Zhifei, R. H. Gonçalves, D. A. Salvatore and C. P. a. M. T. E. Berlinguette, "Electrolysis of CO₂ to Syngas in Bipolar Membrane-Based Electrochemical Cells," *ACS Energy Letters*, vol. 1, no. 6, pp. 1149-1153, 2016.
- [39] C. M. Gabardo, A. Seifitokaldani, J. P. Edwards, C.-T. Dinh, T. Burdyny, M. G. Kibria, O'Brien, C. P. and a. D. S. Edward H. Sargent, "Combined high alkalinity and pressurization enable efficient CO₂ electroreduction to CO," *Energy & Environmental Science*, vol. 11, no. 2018, p. 2531–2539.
- [40] P. Millet, R. Ngameni, S. Grigoriev, N. Mbemba, F. Brisset, A. Ranjbari and C. Etiévant, "PEM water electrolyzers: From electrocatalysis to stack development," *International Journal of Hydrogen Energy*, vol. 35, no. 10, pp. 5043-5052, 2010.
- [41] G. O. Larrazábal, P. Strøm-Hansen, J. P. Heli, K. Zeiter, K. T. Therkildsen, Chorkendorff and B. and Seger, "Analysis of Mass Flows and Membrane Cross-over in CO₂ Reduction at High Current Densities in an MEA-Type Electrolyzer," *ACS Applied Materials & Interfaces*, no. 11, pp. 41281-41288, 2019.
- [42] D. Salvatore, "Electrocatalytic CO₂ conversion in flow reactors," *University of British Columbia*, 2020.
- [43] B. Endrődi, B. Gábor, D. Ferenc, R. Jones, R. Krishnan and J. and Csaba, "Continuous-flow electroreduction of carbon dioxide," *Progress in Energy and Combustion Science*, vol. 62, pp. 133-154, 2017.
- [44] L.-C. Weng and A. T. a. W. A. Z. Bell, "Towards membrane-electrode assembly systems for CO₂ reduction: a modeling study," *Energy & Environmental Science*, vol. 12, no. 6, pp. 1950-1968, 2019.
- [45] H. Yano, F. Shirai, M. Nakayama and K. Ogura, "Efficient electrochemical conversion of CO₂ to CO, C₂H₄ and CH₄ at a three-phase interface on a Cu net electrode in acidic solution.," *Journal of Electroanalytical Chemistry*, vol. 519, no. 1-2, pp. 93-100, 2002.
- [46] L.-C. A. T. B. a. A. Z. W. Weng, "Modeling gas-diffusion electrodes for CO₂ reduction.," *Physical Chemistry Chemical Physics*, vol. 20, no. 25, pp. 16973-16984, 2018.
- [47] H. D. a. H. Y. J. Q. Wang, "Development of rolling tin gas diffusion electrode for carbon dioxide electrochemical reduction to produce formate in aqueous electrolyte," *Power Sources*, vol. 271, p. 278–284, 2014.
- [48] B. Kim, F. Hillman, M. Ariyoshi and S. F. a. P. J. A. Kenis, "Effects of composition of the micro porous layer and the substrate on performance in the electrochemical reduction of CO₂ to CO," *Power Sources*, vol. 312, p. 192–198, 2016,.

- [49] "Bipolar membranes: A review on principles, latest developments, and applications," *Journal of Membrane Science*, vol. 118538, no. Pärnamäe, R.; Mareev, S. V. ; Nikonenko, S. ; Melnikov, N. ; Sheldeshov, V. ; Zabolotskii, H. V. ; Hamelers, M. and Tedesco, M. , 2020.
- [50] D. Y. Xuan and J. Leung, *Micro & nano-engineering of fuel cells*, Crc Press, 2015.
- [51] Y. Li, Z. Yan, J. Hitt, R. Wycisk, P. Pintauro and T. Mallouk, "Bipolar membranes inhibit product crossover in CO₂ electrolysis cells," *Adv. Sustainable Syst*, vol. 2, p. 1700187, 2018.
- [52] M. J. W. L. W. Z. J.-J. Z. F. J. J.-J. Lv, "A highly porous copper electrocatalyst for carbon dioxide reduction," *Adv. Mater.*, p. 1803111, 2018.
- [53] L. H. M. S. C. X. M. Lin, "An experimental- and simulation-based evaluation of the CO₂ utilization efficiency of aqueous-based electrochemical CO₂ reduction reactors with ion-selective membranes," *ACS Appl. Energy Mater.*, vol. 2, pp. 5843-5850, 2019.
- [54] S. Verma, Y. Hamasaki, C. Kim, W. Huang, S. Lu, H. Jhong, A. Gewirth, T. Fujigaya, N. Nakashima and P. Kenis, "Insights into the low overpotential electroreduction of CO₂ to CO on a supported gold catalyst in an alkaline flow electrolyzer," *ACS Energy Lett.*, vol. 3, pp. 193-198, 2018.
- [55] "Sigracet 39 BC," Fuel Cell Store, [Online]. Available: <https://www.fuelcellstore.com/sigracet-39bc>.
- [56] A. Goyal, M. Giulia and A. M. a. K. M. T. Vladislav, "Competition between CO₂ reduction and hydrogen evolution on a gold electrode under well-defined mass transport conditions," *Journal of the American Chemical Society*, vol. 142, pp. 4154-4161, 2020.
- [57] "Complete 5 cm² CO₂ Electrolyzer," Dioxide Materials, [Online]. Available: <https://dioxidematerials.com/product/complete-5-cm-electrolyzer-test-cell/>.
- [58] T. Burdyny and A. S. Wilson, "CO₂ reduction on gas-diffusion electrodes and why catalytic performance must be assessed at commercially-relevant conditions.," *Energy & Environmental Science*, vol. 12, no. 5, pp. 1442-1453., 2019.
- [59] S. Aryal, "Gas chromatography- definition, principle, working, uses," 2018. [Online].
- [60] "Potentiostat galvanostat PARSTAT® MC series," Direct Industry, [Online]. Available: <https://www.directindustry.com/prod/princeton-applied-research/product-119491-1700067.html>.
- [61] C. W. G. R. a. R. W. J. Welty, *Fundamentals of Momentum, Heat, and Mass Transfer*, 5th edition, Wiley, Hoboken, NJ, 2007.
- [62] A. S. P. a. M. M. Kumar, "COMSOL Multiphysics® Modeling in Darcian and Non-Darcian Porous Media," in *Proceedings of the 2016 COMSOL Conference*, Bangalore, India., 2016.
- [63] B. Endrődi, E. Kecsenovity, A. Samu, F. Darvas, R. V. Jones, V. Török and C. Janáky, "Multilayer electrolyzer stack converts carbon dioxide to gas products at high pressure with high efficiency.," *ACS energy letters*, vol. 4, pp. 1770-1777.
- [64] G. O. Larrazábal, P. Strøm-Hansen, J. P. Heli, K. Zeiter, K. T. Therkildsen, I. Chorkendorff and B. Seger, "Analysis of mass flows and membrane cross-over in CO₂ reduction at high current densities in an MEA-type electrolyzer.," *ACS applied mate.*, 2019.
- [65] M. E. Leonard, L. E. Clarke, A. Forner-Cuenca, S. M. Brown and F. R. Brushett, "Investigating electrode flooding in a flowing electrolyte, gas-fed carbon dioxide electrolyzer," *ChemSusChem*, vol. 13, pp. 400-411, 2020.

[66] Z. Yin, H. Peng, X. Wei, H. Zhou, J. Gong, M. Huai, L. Xiao, G. Wang, J. Lu and L. Zhuang, "An alkaline polymer electrolyte CO₂ electrolyzer operated with pure water.," *Energy & Environmental Science*, vol. 12, no. 8, pp. 2455-2462., 2019.

Appendix

A. MFM data

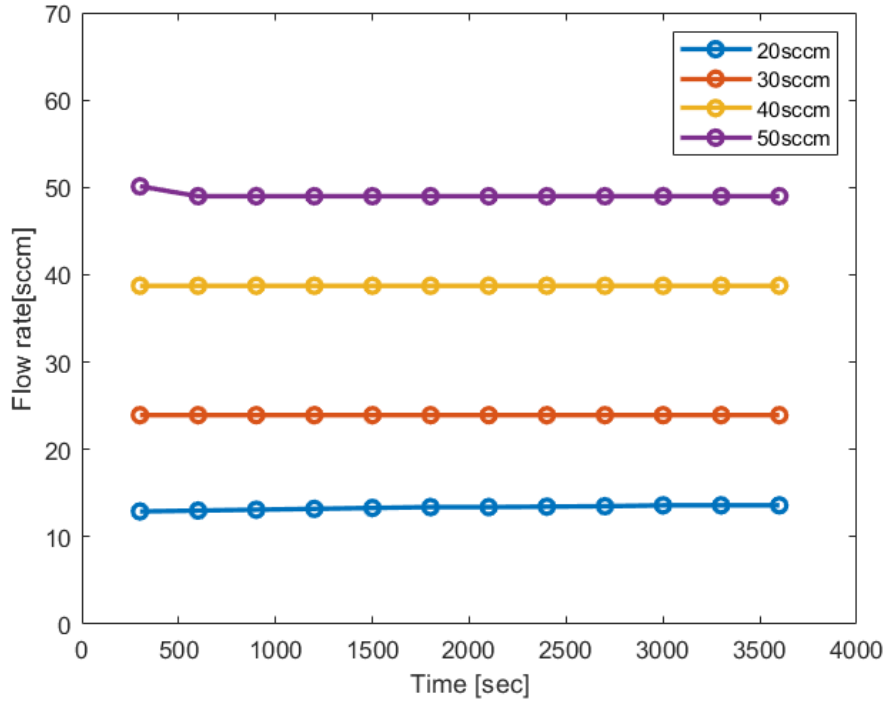


Figure 37: Average outlet mass flow rate after each GC injection; at fixed current density of 50 mA/cm² and variable inlet flow rates

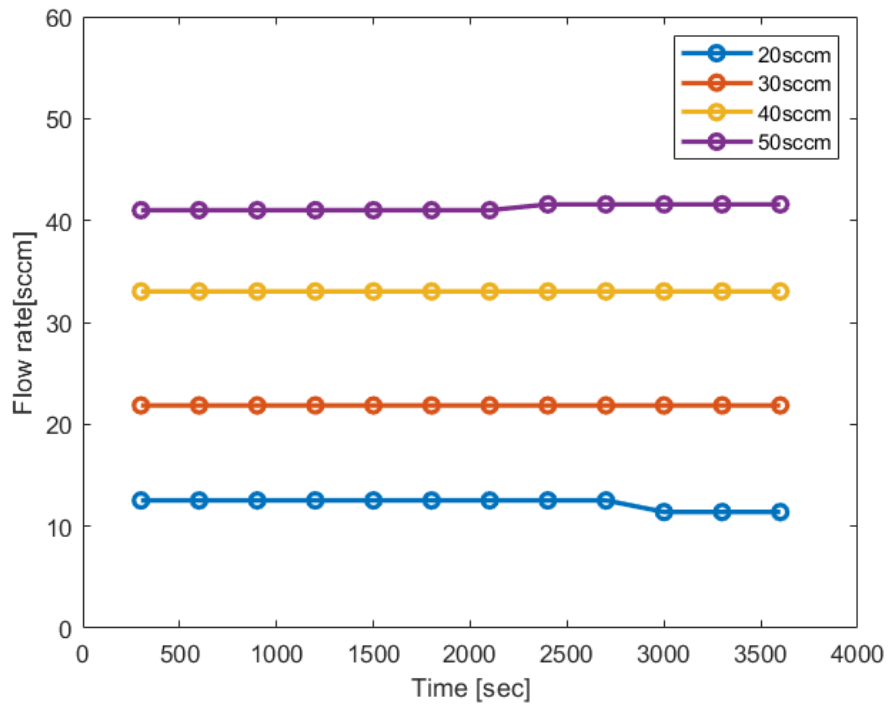


Figure 38: Average outlet mass flow rate after each GC injection; at fixed current density of 150 mA/cm² and variable inlet flow rates.

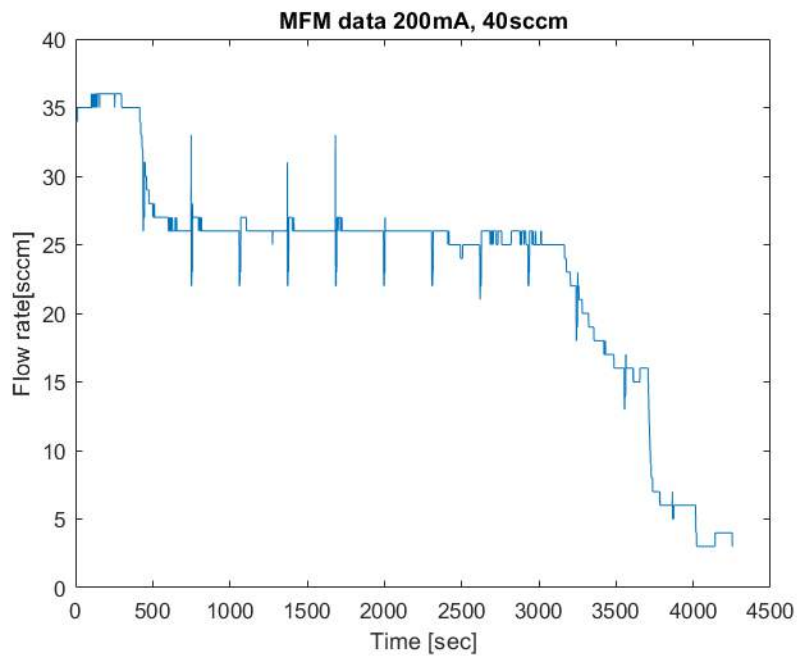


Figure 39: Outlet flow rate versus the time of the experiment at 200mA/cm² and 40sccm

B. Faradaic efficiencies

FE at 20 sccm

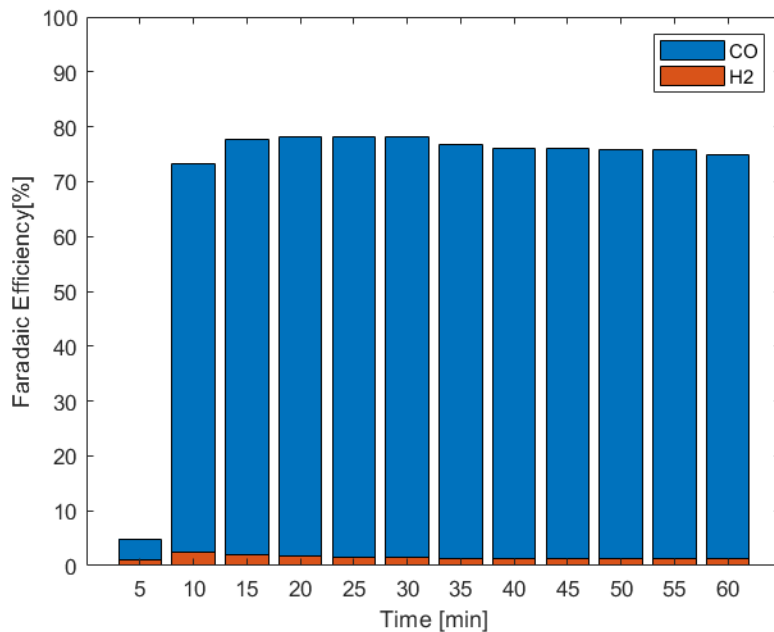


Figure 40 : FE of the gas products of CO₂RR on Ag sample at 50 mA/cm² and 20 sccm.

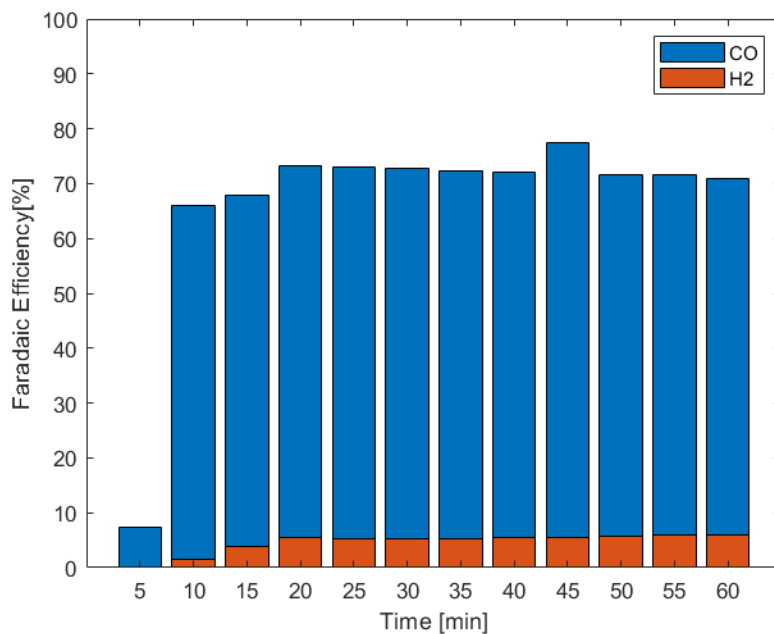


Figure 41: FE of the gas products of CO₂RR on Ag sample at 100 mA/cm² and 20 sccm.

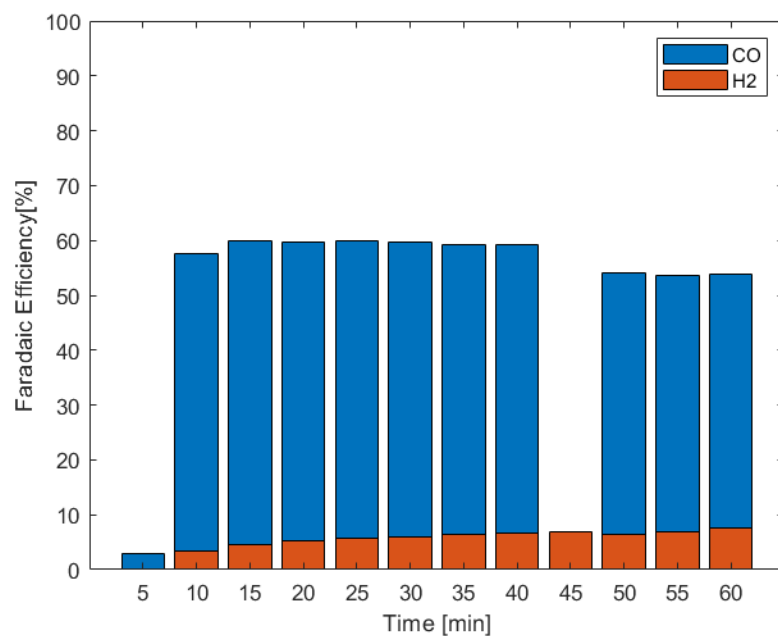


Figure 42: FE of the gas products of CO₂RR on Ag sample at 150 mA/cm² and 20 sccm.

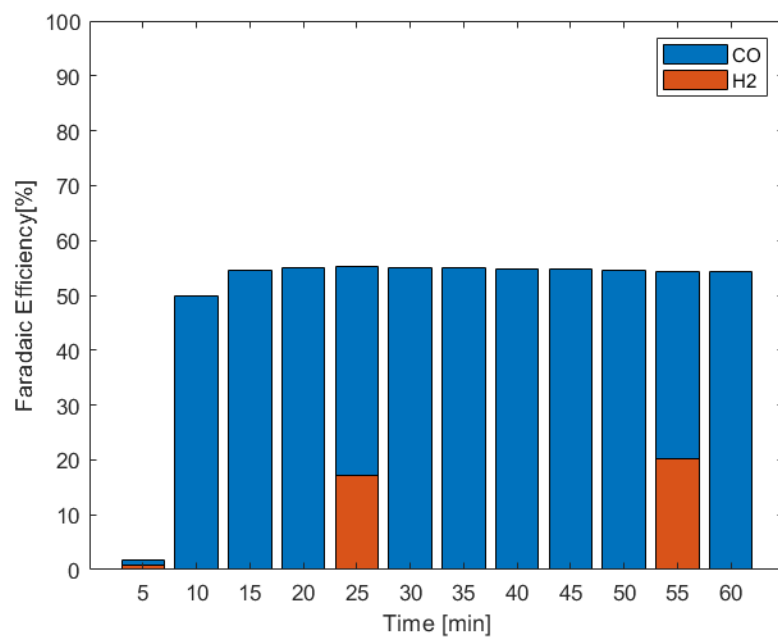


Figure 43: FE of the gas products of CO₂RR on Ag sample at 200 mA/cm² and 20 sccm.

FE at 30 sccm

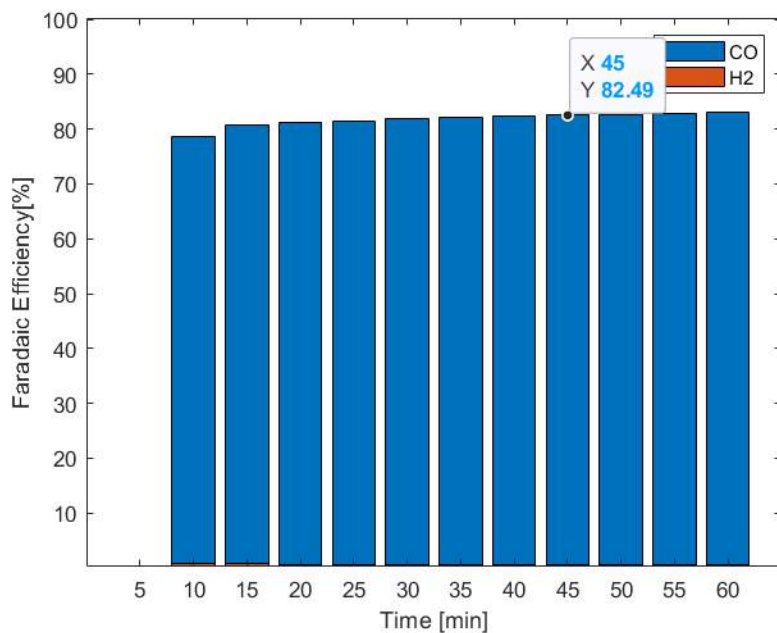


Figure 44: FE of the gas products of CO₂RR on Ag sample at 50 mA/cm² and 30 sccm.

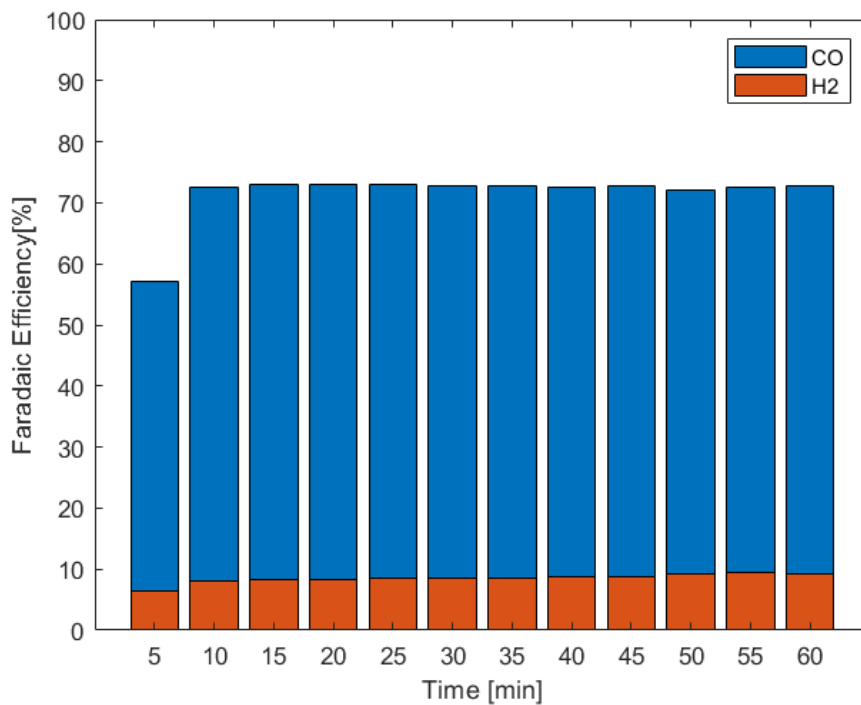


Figure 45: FE of the gas products of CO₂RR on Ag sample at 100 mA/cm² and 30 sccm.

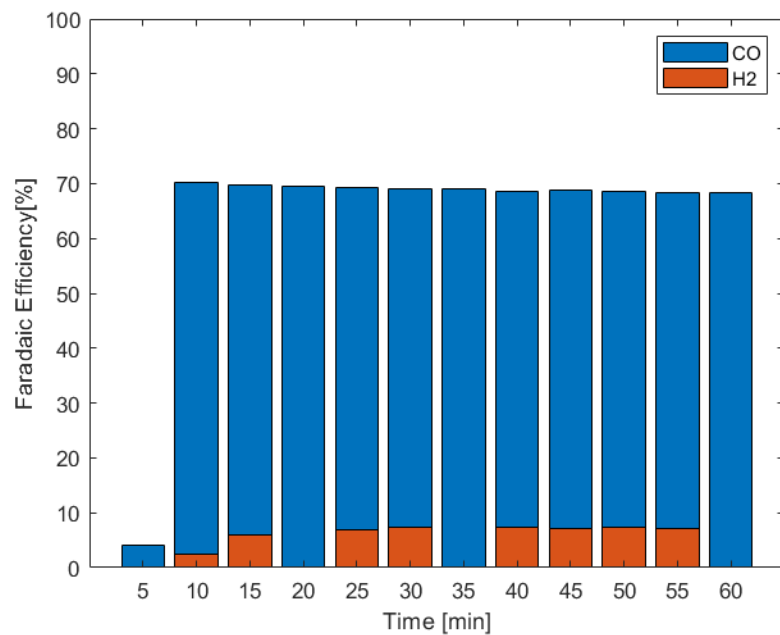


Figure 46: FE of the gas products of CO₂RR on Ag sample at 150 mA/cm² and 30 sccm.

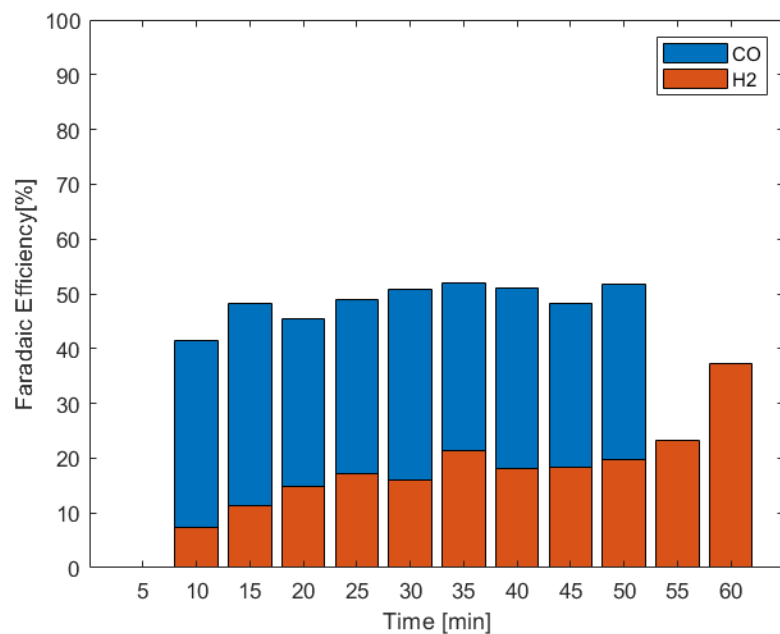


Figure 47: FE of the gas products of CO₂RR on Ag sample at 200 mA/cm² and 30 sccm.

FE at 40 sccm

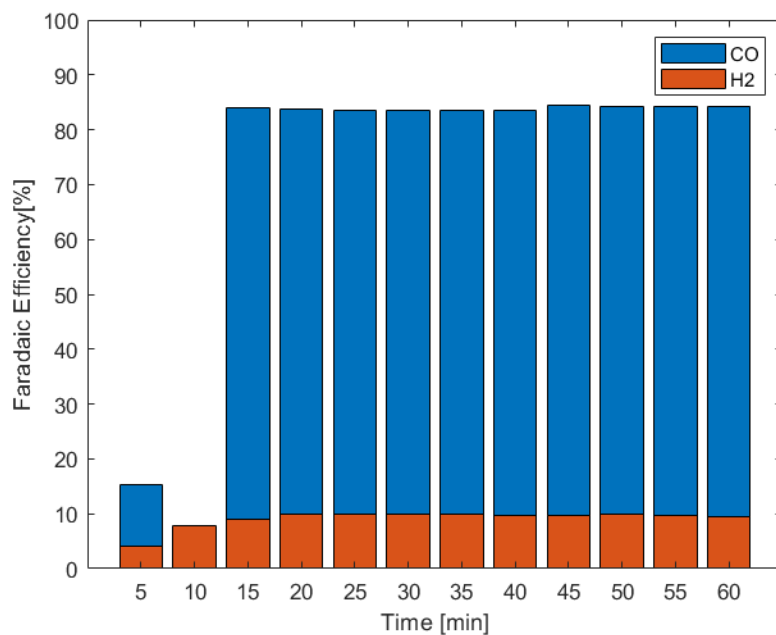


Figure 48: FE of the gas products of CO₂RR on Ag sample at 50 mA/cm² and 40 sccm.

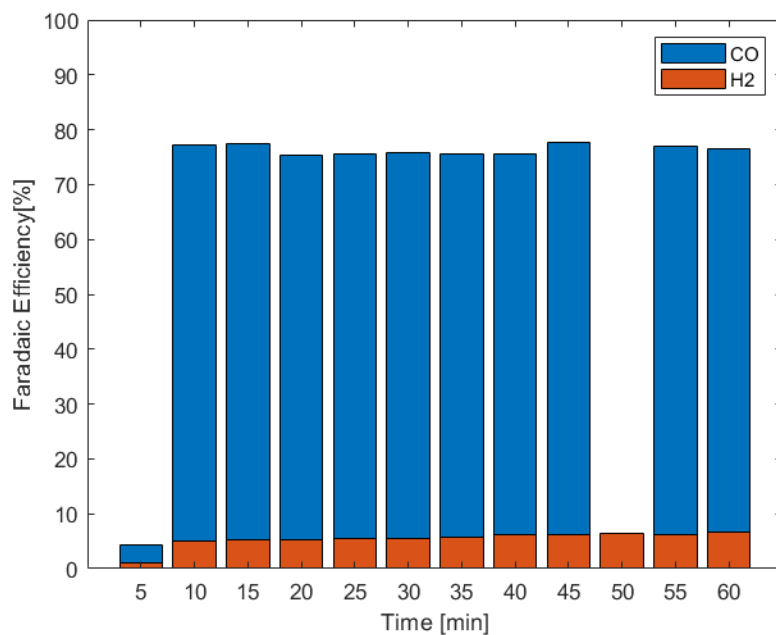


Figure 49: FE of the gas products of CO₂RR on Ag sample at 100 mA/cm² and 40 sccm.

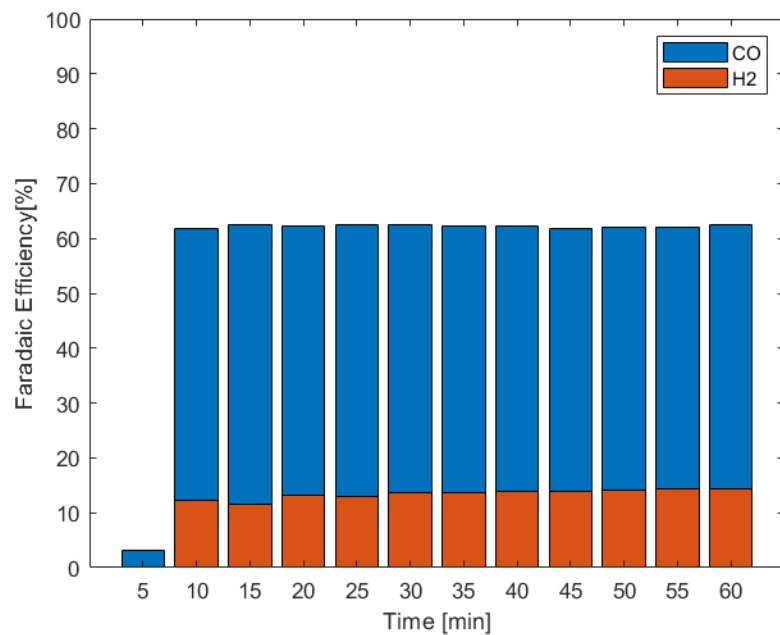


Figure 50: FE of the gas products of CO₂RR on Ag sample at 150 mA/cm² and 40 sccm.

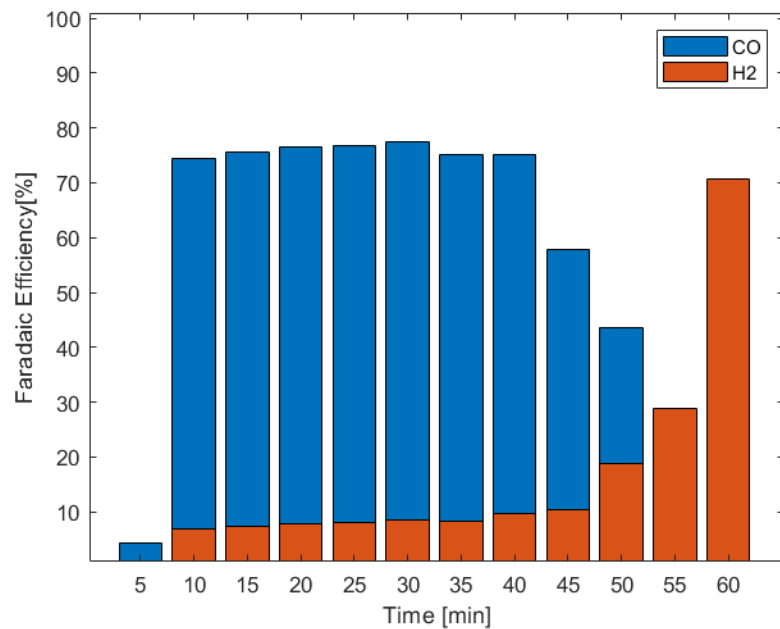


Figure 51: FE of the gas products of CO₂RR on Ag sample at 200 mA/cm² and 40 sccm.

FE at 50 sccm

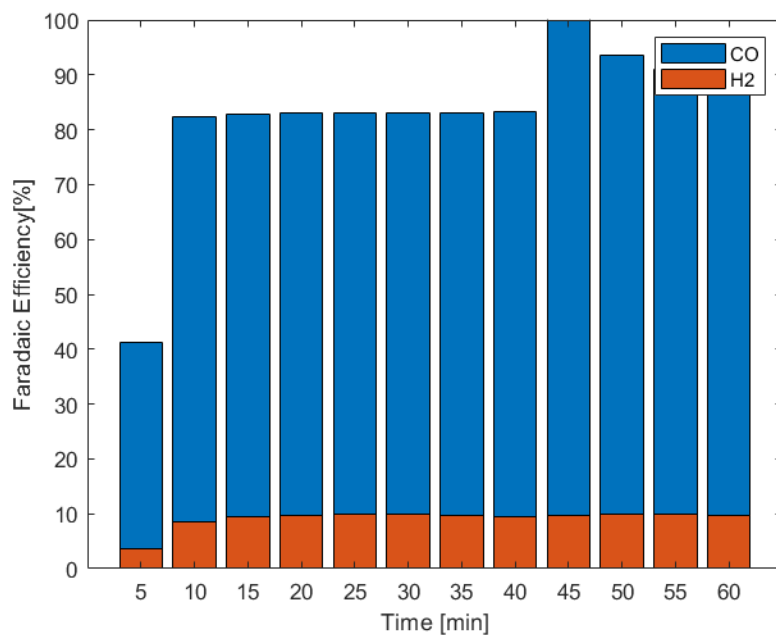


Figure 52: FE of the gas products of CO₂RR on Ag sample at 50 mA/cm² and 50 sccm.

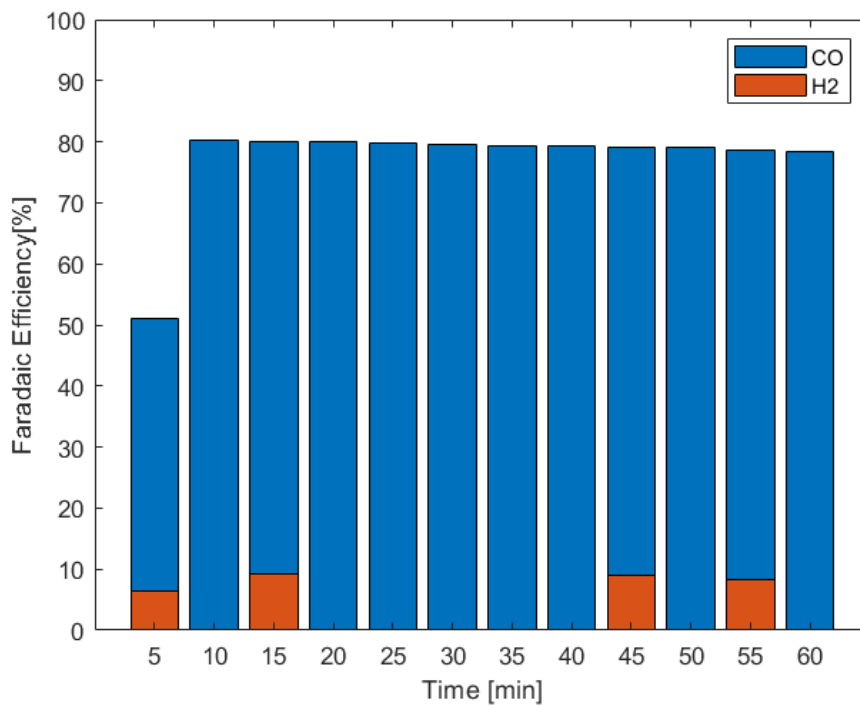


Figure 53: FE of the gas products of CO₂RR on Ag sample at 100 mA/cm² and 50 sccm.

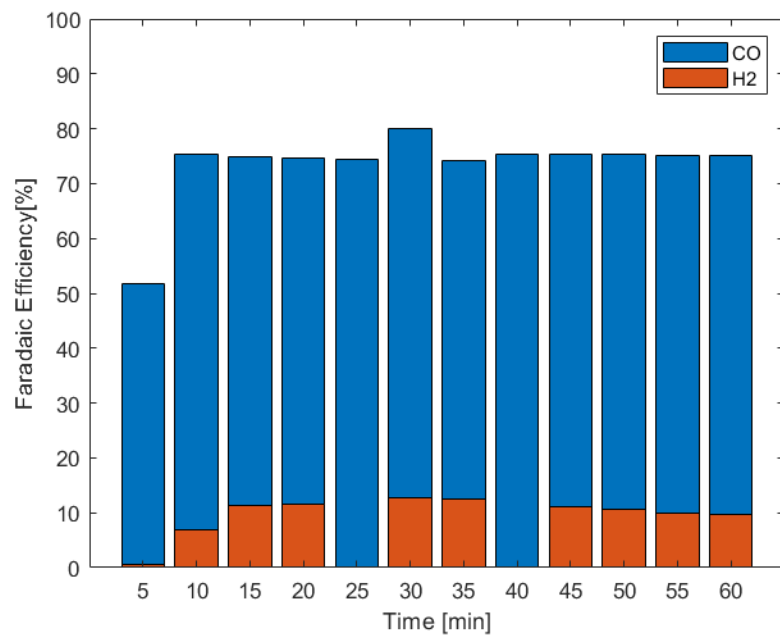


Figure 54: FE of the gas products of CO₂RR on Ag sample at 150 mA/cm² and 50 sccm.

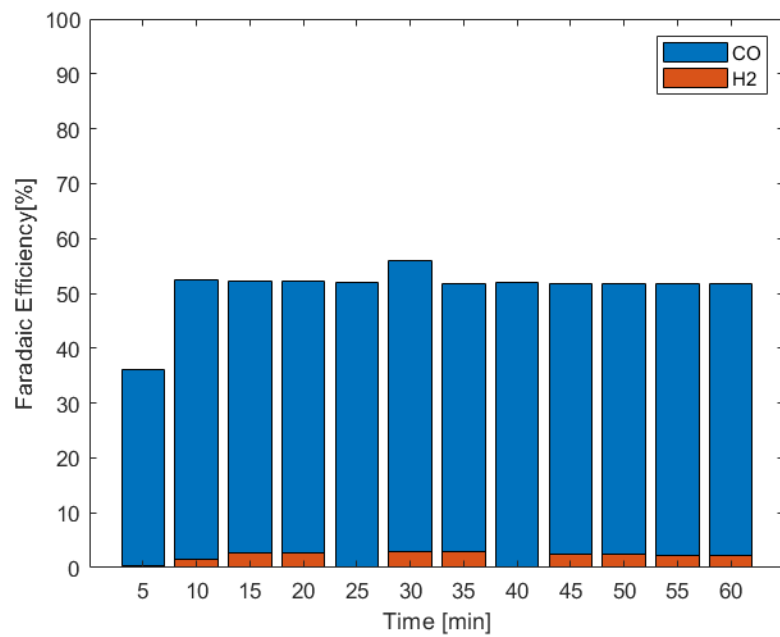


Figure 55: FE of the gas products of CO₂RR on Ag sample at 200 mA/cm² and 50 sccm.

C. Average cell potentials

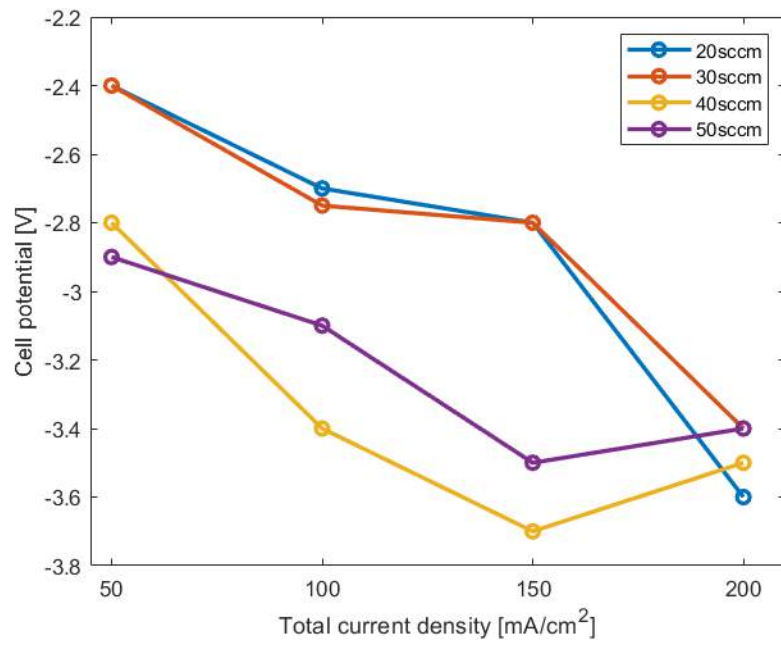


Figure 56: Average cell potentials versus total current densities of all experiments